

Hall effect and symmetry breaking in non-magnetic metal with dynamic charge stripes

N. Sluchanko¹, A. Azarevich¹, A. Bogach¹, S. Demishev¹, K. Krasikov¹, V. Voronov¹,
V. Filipov², N. Shitsevalova², V. Glushkov¹

¹ A.M. Prokhorov General Physics Institute of the Russian Academy of Sciences, 38 Vavilov Str., 119991 Moscow, Russia

² Frantsevich Institute for Problems of Materials Science, National Academy of Sciences of Ukraine, 3 Krzhyzhanovsky Str., 03680 Kyiv, Ukraine

A comprehensive study of magnetoresistance and Hall effect has been performed for the set of the single crystals of non-magnetic metal LuB_{12} with the Jahn-Teller instability of the boron cage and dynamic charge stripes forming along $\langle 110 \rangle$ direction. Anomalous positive contribution to Hall effect for particular direction of magnetic field $\mathbf{H} // [001]$ is found in the single crystals of LuB_{12} of the highest quality. This contribution arising at $T \sim 150$ K is shown to increase drastically when approaching the disordered ground state below 60 K. The Hall effect anomaly is shown to appear in combination with the peak of magnetoresistance. The various scenarios allowing for the topology of Fermi surface, anisotropy of relaxation time for charge carriers and the filamentary structure of fluctuating charge stripes are proposed to explain the features of magnetotransport in this metal with inhomogeneous distribution of electron density. The origin of SdH oscillations, which are observed in this non-equilibrium metal with electron phase separation and strong charge carrier scattering, is discussed.

PACS numbers: 72.15.Gd, 72.20. My

1. Introduction. The unique opportunity for studying of the features of electron phase separation in strongly correlated electron systems is provided by dynamic, or fluctuating charge and spin stripes, which attract extraordinary scientific interest due to their important role in the mechanism of high temperature superconductivity (HTSC, see, e.g., [1-14]). While the stripe states are generally considered as a special feature for the $\text{La}_{2-x}\text{Ba}_x\text{CuO}_4$ perovskite family [15], phase singularities accompanied by lowered symmetry of the lattice are detected in other cuprates ($\text{YBa}_2\text{Cu}_3\text{O}_{7-\delta}$ [16-17], $\text{SmBa}_2\text{Cu}_3\text{O}_x$ [18], $\text{Bi}_2\text{Sr}_2\text{CaCu}_2\text{O}_{8+\delta}$ [19] and $\text{Ca}_{2-x}\text{Na}_x\text{CuO}_2\text{Cl}_2$ [20]). This kind of electron instability is also suggested to be extremely important for understanding of exotic physics in colossal magnetoresistive manganites [21-22], nickelates [23-25], iron-based superconductors [26-27], heavy fermion hexaborides [28], etc.

An especial kind of fluctuating charge stripes have been recently detected in the non-magnetic dodecaboride LuB_{12} [29,30,31] and magnetic $\text{Tm}_{1-x}\text{Yb}_x\text{B}_{12}$ compounds with metal-insulator transition [32]. The mechanism responsible for this electron and lattice instability in RB_{12} with *fcc* crystal structure is related to dynamic cooperative Jahn-Teller (JT) effect in the B_{12} clusters [29,31]. It was shown in [29] that, because of triple orbital degeneracy of the ground electronic state, the B_{12} molecules are JT active and their structure is labile due to JT distortions. The quantum chemical calculations and geometry optimizations for the charged $[\text{B}_{12}]^{2-}$ cluster, which doubly negative charge state is regarded as the most relevant one in RB_{12} compounds [29], allow concluding in favor of strong trigonal and tetragonal distortions of the *fcc* lattice and mixture via a non-adiabatic electron-vibronic coupling of electronic states for each B_{12} cluster [33]. In the dodecaboride matrix (see fragment of the *fcc* crystal structure in Fig.1a), the *collective JT effect* in the lattice of these B_{12} complexes is the origin of both the collective dynamics of boron clusters and large amplitude vibrations (rattling modes) of the rare earth ions embedded in B_{24} cavities of the boron cage (see Fig.1b). Strong coupling of these Lu rattling modes located at 110 cm^{-1} ($\sim 14 \text{ meV}$) [34] and the JT active vibrations of boron are the origin of

both lattice instability and the emergence of the collective excitations in the optical spectra of LuB_{12} [35].

The Lu rattling modes correspond to Einstein oscillators in the double-well potential (Fig.1c). The large amplitude of these rattling modes initiates strong changes in the *hybridization* of rare earth and boron electron states. Since the states in the conduction band are contributed by the $2p$ orbitals of B_{12} and the $5d$ orbitals of Lu [36, 37, 38, 39], the variation of the $5d-2p$ hybridization leads to the modulation of conduction band width and, consequently, may generate non-equilibrium (“hot”) electron states. These charge carriers seem to amount by $\sim 70\%$ from the total number of conduction electrons as estimated from overdamped oscillators in the optical conductivity spectra at room temperature [35]. Due to the stripe formation a considerable part of non-equilibrium conduction electrons is accumulated in the filamentary structure of fluctuating charges (see wide green channels in Fig.1a [30]). Note also that the lattice and electron systems of LuB_{12} are significantly modified below $T^* \sim 60$ K where the cage-glass state [40] is formed due to positional disorder of the loosely bound Lu^{3+} ions embedded in B_{24} truncated cubooctahedrons caused by static displacements of R^{3+} ions in the double-well potential (Fig.1b-c).

The investigation of crystal structure, heat capacity and charge transport [31] allowed to argue that in the family of $\text{Lu}^{\text{N}}\text{B}_{12}$ crystals with various boron isotopes $\text{N}=10, 11, \text{nat}$ (the last index corresponds to the natural mixture of 18.8% ^{10}B and 81.2% ^{11}B) $\text{Lu}^{\text{nat}}\text{B}_{12}$ possesses the strongest local atomic disordering in combination with long-range JT trigonal distortions. These factors provide optimal conditions for the formation of the dynamic charge stripes below $T^* \sim 60$ K. As a result, the resistivity and Seebeck coefficient of the $\text{Lu}^{\text{nat}}\text{B}_{12}$ heterogeneous medium decrease strongly in comparison with those ones detected for pure boron isotope crystals. It was concluded in [31] that any defects are supposedly used as the pinning centers facilitating the formation of additional quantum conductive channels (dynamic charge stripes) in the metallic matrix of RB_{12} .

Hall effect is usually considered as a key experiment to reveal a transformation of electron spectrum in the vicinity of quantum critical point (QCP) [41-44], in the stripe-ordered compounds [45-46], near the metal-insulator transition [47-49], etc. All the singularities were detected in the $Tm_{1-x}Yb_xB_{12}$ family [50, 32] and the complicated behavior of the Hall resistivity components was interpreted in terms of both the metal-insulator transition and electron phase separation effects in combination with formation of nanoclusters of the rare earth ions in the cage-glass state of the studied compounds. The instability of Yb 4*f*-electron configuration in these Yb-based rare-earth dodecaborides is developed in combination with the JT deformations of the boron cage (Yb ion valence is about 2.92-2.95 [51-52]). This phenomenon provides one more mechanism of the charge and spin fluctuations in RB_{12} and it is promising to separate only the influence of dynamic charge stripes on the Hall voltage anomalies in RB_{12} . In this study we present the results of detailed Hall effect measurements of different quality single crystals of the non-magnetic reference compound LuB_{12} . We show here that an ordinary Hall effect in LuB_{12} is modified by the appearance of specific contribution to the Hall resistivity, which could not be explained exclusively in terms of anisotropic Fermi surface and is suggested to be caused by an interaction of the dynamic charge stripes with external magnetic field.

2. Experimental details.

2.1. Crystal growth. The single crystals of non-magnetic LuB_{12} dodecaboride were grown using the induction crucible-free zone melting method with multiple re-melting in an argon gas atmosphere from the preliminarily synthesized LuB_{12} powders [53]. All the crystals under investigation (#1-6) have been grown from the initial high purity LuB_{12} powder synthesized from the 4N lutetium oxide Lu_2O_3 (99.9985 wt. % purity, particle size less than 100 microns) and 3N amorphous boron (99.9 wt. % purity, particle size about 50 Å). The details of both ingot preparation and solid state reaction are given in [54]. Different technological regimes were applied during the growing process. In the case of crystal # 1, an additional purification of argon

from possible contamination of other gases was carried out directly in the growth chamber where Ti was used as a getter. The crystals #1-2 and #4-6 were grown with single zone passing under different pressures of argon gas ranging from 0.15 to 0.5 MPa with equal crystallization rates. The crystal #3 with the highest residual resistivity value was grown with triple zone passing. Perfect x-ray diffraction reflexes in Laue pattern (for crystals #1-6) and quantum oscillations of the magnetization (de Haas-van Alphen effect) observed in magnetic field $\mathbf{H} \parallel [100]$ (for crystals #1) prove the high quality of the crystals under investigation.

2.2. Galvanomagnetic measurements.

The samples for magnetoresistance (MR) and Hall effect (HE) measurements were cut from the single domain crystals oriented along the principal crystallographic directions with accuracy $\sim 2^\circ$, then these were polished and etched to delete the distorted surface layer. The angular dependences of resistivity and Hall voltage were measured by the original sample rotation technique with a stepwise ($\Delta\varphi=1.8^\circ$) fixing of the sample position in the steady magnetic field. The magnetic field supplied by superconducting solenoid up to 80 kOe was applied perpendicular to the measuring direct current (DC) $\mathbf{I} \parallel \langle 110 \rangle$ in #1-#6 (see inset in Fig. 5a below, the orientation of the normal vector $\mathbf{n} \parallel \langle 001 \rangle$, or $\mathbf{n} \parallel \langle 110 \rangle$ was used). For the samples #1 the resistivity and Hall effect measurements were carried out also in the magnetic field up to 140 kOe at liquid helium temperature (sample 1a, $\mathbf{I} \parallel [110]$) and for #1 and #2 in various DC directions (samples #1b and #1c with $\mathbf{I} \parallel [100]$ and $\mathbf{I} \parallel [010]$, correspondingly). The installation equipped with a step-motor with automated control of the step-by-step sample rotation is similar to that one applied previously in [50]. High accuracy of the temperature control ($\Delta T \approx 0.002\text{K}$ in the range 1.8-7K) and magnetic field stabilization ($\Delta H \approx 2\text{ Oe}$) was achieved by using the commercial temperature controller TC 1.5/300 and superconducting magnet power supply unit SMPS 100 (Cryotel Ltd.) in combination with CERNOX 1050 thermometer (Lake Shore Cryotronics, Inc.) and Hall sensors.

3. Experimental results and analysis.

3.1. Temperature dependences ($\mathbf{H} // \langle 110 \rangle$). Fig. 2 shows the metallic type temperature dependences of resistivity $\rho(T)$ measured for various LuB_{12} single crystals. The temperature independent “plateau” is observed on the $\rho(T)$ curves in the range $T \leq 20$ K for all the studied crystals. The residual resistivity ratio ($\text{RRR} = \rho(300 \text{ K})/\rho(4.2 \text{ K})$) varies about by the factor of 6 from ~ 70 (sample #1) to ~ 12 (sample #3). The resistivity $\rho(T, H_0)$ and the reduced Hall resistivity $\rho_H/H = f(T, H_0)$ have been studied in detail in magnetic field $H_0 = 80$ kOe for samples #1, #2 and #3 in two orientations $\mathbf{H} // [100]$ and $\mathbf{H} // [110]$ (see Fig.3). Taking into account the electron density inhomogeneity in LuB_{12} due to dynamic charge stripes found in the dodecaboride matrix [30] (see Fig. 1a), the term “reduced Hall resistivity” $\rho_H/H = f(T, H_0)$ will be used below instead of Hall coefficient $R_H(T, H_0) \equiv \rho_{xy}/H$. Fig. 3 presents the data of Hall resistivity measured for two opposite directions of external magnetic field $\pm \mathbf{H} // \mathbf{n}$ and calculated applying the general relation $\rho_H = [(V_H(H) - V_H(-H))/(2I)]d$ (V_H is the voltage from the Hall probes and d is the thickness of the sample or, equivalently, its size along the normal direction to the largest face). For the sample #1a strong MR anisotropy is clearly seen in Fig.3a with a maximum values detected for $\mathbf{H} // [100]$ and it is accompanied with a dramatic decrease of the absolute values of ρ_H/H with the temperature lowering (Fig.3b). On the contrary, the reduced Hall resistivity ρ_H/H for $\mathbf{H} // [110]$ reveals only moderate changes with a negative minimum at the cage-glass transition temperature $T^* \sim 60$ K [40]. Thus, the values of ρ_H/H in crystal #1a differ by more than 3 times for these two directions of magnetic field. Simultaneously both the MR anisotropy and the strong temperature variation of the reduced Hall resistivity ρ_H/H for $\mathbf{H} // [100]$ depress essentially with the increase of residual resistivity ρ_0 in the sample #2 (Fig. 3 c,d). This low temperature anisotropy becomes very small in the sample #3 (Fig.3 e,f) with the highest ρ_0 value (shortest mean free path of the charge carriers). Taking into account that the Hall coefficient of normal uncompensated metal in strong magnetic fields is determined by the difference of electron and hole concentrations of $R_H = \rho_H/H \sim (n_e - n_h)^{-1}$ [55,56] it is extremely

unusual to observe such a strong anisotropy of the reduced Hall resistivity ρ_H/H for the highest quality crystal (#1a) in the LuB_{12} family (#1-#6).

Fig. 2b demonstrates the temperature dependences of Hall mobility $\mu_H(T) = (\rho_H(T)/H) / \rho(T)$ estimated for the crystals #1, #2 and #3 for two directions $\mathbf{H} // [100]$ and $\mathbf{H} // [110]$. It is worth noting that unusually strong difference between $\mu_H(\mathbf{H} // [100])$ and $\mu_H(\mathbf{H} // [110])$ (about 6 times) appears for the sample #1a just below $T^* \sim 60$ K in the disordered cage-glass phase of LuB_{12} . The ratio $\mu_H(\mathbf{H} // [100]) / \mu_H(\mathbf{H} // [110])$ is reduced by a factor of 3 for sample #2 and becomes as low as 1.1 in the case of the sample #3. The exponential behavior of Hall mobility $\mu_H(T) \sim T^{-\alpha}$ is observed in the temperature range 80-300 K for all LuB_{12} crystals; the $\alpha \approx 7/4$ exponent is detected for the samples #1 and #2 with the large values of $\text{RRR} = 40-70$ and $\alpha \approx 3/2$ is estimated for the sample #3 ($\text{RRR} \sim 12$) (Fig.2b). Note that the $\alpha = 3/2$ exponent is typical for the scattering of conduction electrons by acoustic phonons (deformation potential) and the increase of α values up to $7/4$ in the crystals #1 and #2 means that other scattering channels contribute mainly to the relaxation processes of charge carriers in the clean limit of LuB_{12} . The details of the phonon spectra of LuB_{12} have been detected in [34] allowing to conclude in favor of the dominant carriers scattering on the quasi-local vibrations of the RE ions. So, relaxation processes due to scattering on both the boron optical phonons [34] in the presence of the JT distortions and the rattling modes of the RE ions [29-31] may be considered as dominant factors, which are responsible for the observed α increase in the samples #1 and #2 of the RE dodecaboride with JT instability of the boron sub-lattice.

3.2. Magnetic field sweeping ($\mathbf{I} // \langle 110 \rangle$). The magnetic field dependences of reduced Hall resistivity $\rho_H/H = f(H)$ (Fig.4a), resistivity $\rho(H)$ (Fig.4b) and Hall mobility $\mu_H(H)$ (Fig.4c) show the results obtained for the sample #1a at $T = 4.2$ K (see also Supplementary Information [54] for other LuB_{12} crystals). For $\mathbf{H} // [100]$ the amplitude of the reduced Hall resistivity demonstrates a dramatic (~ 10 times) decrease with the rise of magnetic field up to 140 kOe, and, on the

contrary, for $\mathbf{H}//[110]$ the amplitude of $\rho_H/H=f(H)$ increases only slightly. It is worth noting that the low-field values of ρ_H/H for $\mathbf{H}//[110]$ and $\mathbf{H}//[100]$ are just equal to each other (Fig.4a), so any noticeable discrepancy is developed only above 10 kOe. Straightforward estimations of Hall mobility for the highest quality crystal #1a from the data of Figs.4a and 4b result in high enough values of $\mu_H \sim 3000 \text{ cm}^2/(\text{V s})$ in low fields and small values of $\mu_H(H \approx 140 \text{ kOe}) \sim 18 \text{ cm}^2/(\text{V s})$ in high fields for $\mathbf{H}//[100]$ at liquid helium temperature. Note, that the last values are about 40 times smaller than those ones detected for $\mathbf{H}//[110]$ (Fig.4c). This observation proves that simple free electron model fails to extract any real microscopic parameters of charge carriers from the experimental data. Taking into account values of Fermi velocity $v_F \approx 1.1 \cdot 10^7 \text{ cm/s}$ [35] and the effective mass $m^* \sim 0.5 m_0$ [38] small enough average mean free path of charge carriers $l \sim 350 \text{ \AA}$ may be estimated even in the best quality single crystal #1 of LuB_{12} . It is worth noting also that the difference between estimated Hall mobilities for $\mathbf{H}//[100]$ and $\mathbf{H}//[110]$ decreases strongly for the sample #2 with $\mu_H(H < 10 \text{ kOe}) \sim 1500 \text{ cm}^2/(\text{V s})$ and becomes much smaller for the sample #3 where $\mu_H(H < 10 \text{ kOe}) \sim 420 \text{ cm}^2/(\text{V s})$ (see [54] for more detail) giving evidence for strong degradation of mean free path in the #1-#2-#3 series.

3.3. Transverse MR anisotropy ($\mathbf{I} // \langle 110 \rangle$). The anisotropy of the transverse MR $\Delta\rho/\rho$ in LuB_{12} at liquid helium temperature is analyzed by discussing of (i) the magnetic field dependences of magnetoresistance collected at different fixed angles φ between the normal \mathbf{n} to the (100) surface and the applied magnetic field ($\angle\varphi = (\mathbf{n} \wedge \mathbf{H})$, see the inset of Fig. 5a) and (ii) the angular dependence of magnetoresistance measured in various magnetic fields up to 80 kOe. The data of field and angle sweeping measurements for the sample #1a are shown in Figs. 5a and 5b, respectively. For comparison, Fig. 5c shows the anisotropy of MR detected for several LuB_{12} crystals having different RRR values (from 12 to 70) and the liquid helium Hall mobility ranging as $420\text{-}3000 \text{ cm}^2/(\text{V s})$ (see Fig.4 and the data in [54]). It is easy to see that a whole set of extrema with small enough values of MR is detected on the $\Delta\rho/\rho(\varphi)$ dependences in the angle range $54^\circ < \varphi < 126^\circ$ in the vicinity of the diagonals $\mathbf{H}//[110]$ and $\mathbf{H}//[111]$. At the same time, $\Delta\rho/\rho$

strongly increases within a wide range of angles ($-25^\circ < \varphi < +25^\circ$) when approaching to $\mathbf{H} // [001]$ (Fig. 5b and 5c). Note that the observed anisotropy of transverse magnetoresistance $\Delta\rho/\rho(\varphi)$ is very similar to this one reported earlier for LuB_{12} crystal at 0.5 K in 12 T [38]. This distorted cross-type anisotropy of MR is mostly pronounced in the polar plot shown in Fig. 6a and it could be evidenced either in favor of the existence of an open trajectories on the Fermi surface [38], or, it shows up the presence of the filamentary structure of the dynamic charge stripes in LuB_{12} .

To shed more light on the details of the MR anisotropy in the non-magnetic compound LuB_{12} the angular dependences of $\Delta\rho/\rho(\varphi, T_0, H_0)$ have been studied for the sample #1a in the strong magnetic field $H_0=80$ kOe in the wide temperature range 1.8-200 K. Fig. 6b shows the 3D view of the transverse MR in the cylindrical plot. It is easy to see in Fig.6b that the strongest increase of MR occurs when \mathbf{H} is oriented perpendicular to the filamentary structure of the quantum conduction channels ($\mathbf{H} // [001]$) while only moderate humps of MR are detected in the wide neighborhood of $\mathbf{H} // [110]$ dynamic charge stripe direction. Interestingly, both of the mentioned features are developed just below the cage-glass transition $T^* \sim 60$ K (marked by dotted white line in Fig.6b).

3.4. Angular dependences of Hall resistivity ($\mathbf{I} // \langle 110 \rangle$). The selected angular dependences of reduced Hall resistivity $\rho_H/H = f(\varphi, H_0)$ measured in various magnetic fields at liquid helium temperature are presented for two different orientations of the normal vector $\mathbf{n} // [001]$ and $\mathbf{n} // [110]$ in Figs. 7 and 8, correspondingly (the sample #1a, current axis $\mathbf{I} // [110]$; see also fig.S2 in [54] for the sample #2). The cosine-like behavior of Hall resistivity angular dependences is natural for isotropic non-magnetic metal reflecting the changes of potential difference between two Hall probes due to varying transverse HE electric field (see the schema in the inset in fig.5a). This simplified behavior is really observed for the sample #3 (Figs. 7c, 8c) with smallest RRR, where Hall mobility is less than $450 \text{ cm}^2/(\text{V s})$ (Fig. S3 in [54]). On the contrary, an additional anomalous component contributes to Hall signal for the samples #1a and

#2 in the configuration $\mathbf{I}//[110]$, $\mathbf{n}//[001]$ in the wide neighborhood of $\mathbf{H}//\langle 001 \rangle$ direction (Fig.7). The singularity is strongest for the sample #1a with the largest RRR ($\mu_{\text{H}}(10 \text{ kOe}) \sim 3000 \text{ cm}^2/(\text{V s})$, Fig.4c). Indeed, the magnitude of the anomalous non-harmonic contribution for the sample #1a at $H=80 \text{ kOe}$ compensates substantially of the cosine-like component of the ordinary Hall effect near $\mathbf{H}//\mathbf{n}//[001]$, and the non-harmonic feature depresses for the samples #2 and #3 (see Figs.7a, 7b and 7c, and Fig.S6 in [54]). Moreover, the singularity is not observed when $\mathbf{H}//[110]$ for the same rotation axis ($\mathbf{I}//[1-10]$) and the other $\mathbf{n}//[110]$ configuration). Instead, two additional anomalous features of opposite sign have been detected on the $\rho_{\text{H}}/H=f(\varphi, H_0)$ data in the vicinity of $\mathbf{H}//\langle 111 \rangle$ directions (see Fig.8 for #1a).

The dramatic difference between ρ_{H}/H vs. T (Fig.3) and ρ_{H}/H vs. H (Fig.4) for $\mathbf{H}//[001]$ and $\mathbf{H}//[110]$ detected in our experiments and the qualitative dissimilarity of the $\rho_{\text{H}}/H=f(\varphi, H_0)$ data for $\mathbf{H}//[001]$ and $\mathbf{H}//[110]$ (shown by arrows in Figs.7a and 8a, respectively) make evident that the discovered singularity in the vicinity of $\mathbf{H}//\langle 001 \rangle$ is responsible for very strong changes in the Hall signal observed in the $\mathbf{H}//[001]$ configuration. Indeed, the amplitude of the feature detected near $\mathbf{H}//\langle 001 \rangle$ increases drastically both in magnetic field (see Figs. 7a, 9b) and with temperature decreasing below $T^* \sim 60 \text{ K}$ (see Fig. 9a). It should be pointed out that the anomaly is observed in the sample #1a (see also Fig.S7 in [54] for the sample #2) when the external magnetic field $\mathbf{H}//\langle 001 \rangle$ is applied perpendicular to the $[110]$ direction of dynamic charge stripes (see Fig. 1a). This observation points to the possible relationship between the observed singularity and the effects of interaction of magnetic field with the filamentary structure of the quantum conduction channels. It is worth noting also, that in low magnetic field ($H < 20 \text{ kOe}$) the amplitude of the cosine-like contribution decreases essentially ($\sim 15\%$) in the sample sequence #1- #2- #3 (fig.7), so, it should be suggested that the emergence of the infinite cluster of the dynamic charge stripes is accompanied with the moderate enhancement of the negative ordinary HE. More detailed quantitative analysis and general discussion of HE in LuB_{12} is presented below.

3.5. H-T variation of HE components ($\mathbf{l} // \langle 110 \rangle$). To separate the ordinary and anomalous contributions to Hall effect the experimental data $\rho_H(\varphi, H_0, T_0)$ (Figs. 9a-b and 10) were fitted by cosine law $\rho_{H0}(H_0, T_0)\cos\varphi$ in the segments $90^\circ \pm 20^\circ$ and $270^\circ \pm 20^\circ$ (see, *e.g.*, Fig.9b and 10 for #1a and Fig.S7 in [54] for #2). The difference $\rho_H^{\text{an}}(\varphi, H_0, T_0) = \rho_H(\varphi, H_0, T_0) - \rho_{H0}(H_0, T_0)\cos\varphi$ was attributed to the additional specific component of HE. The temperature and field dependences of the main term $R_H(T, H) \equiv \rho_{H0}/H$ (ordinary Hall effect, marked as “cos”) are shown in Figs. 3b and 4a for the sample #1a, and in Figs. 3d and in [54] for the sample #2. The H-T variation of the additional term $\rho_H^{\text{an}}/H(\varphi, H_0, T_0)$ for $\mathbf{n} // [001]$ configuration is presented in Figs. 9c and 9d for #1a and in Fig.S7 in [54] for #2. Fig. 10 shows the reduced Hall resistivities ρ_H/H and $\rho_H^{\text{an}}/H = f(\varphi, H_0, T_0)$ detected in the $\mathbf{n} // [110]$ configuration of #1a at 4.2K. It is clearly discerned from Figs.9c, 9d that the largest ρ_H^{an}/H is observed for the $\mathbf{n} // [001]$ configuration around the $\langle 001 \rangle$ axis and the positive polarity of the additional specific component is opposite to the negative ordinary contribution in the Hall voltage of LuB_{12} . Besides, this anomalous term consists of two parts – smooth $\Delta_{\text{smooth}}(\varphi, H_0, T_0)$ and step-like $\Delta_{\text{step}}(\varphi, H_0, T_0)$ (see the legend in Figs. 9c, 9d). The data analysis allows detecting the changes in these Δ_{smooth} and Δ_{step} amplitudes both with the temperature variation (Fig. 9e) and magnetic field increasing (Fig.9f). Note that the sum of the specific component and ordinary Hall coefficient within the experimental accuracy is equal to Hall resistivity $\rho_H/H = f(\varphi, H_0, T_0)$ measured without sample rotation as a difference between the data for two opposite directions of magnetic field (see Figs. 3a and 4a), arguing in favor of the proposed explanation of the Hall voltage anomalies in the metal with dynamic charge stripes.

It is easy to see from Figs.9e, 9f that the main specific component Δ_{smooth} appears in the crystals #1 and #2 of LuB_{12} just below $T_E \sim 150$ K, where the development of the JT instability of B_{12} sub-lattice was found previously in various experiments. Indeed, it was shown in Raman studies [40] that temperature lowering leads to a sharp increase in the vibration density of states near T_E when the mean free path of phonons reaches the Ioffe–Regel limit and becomes

comparable with their wavelength [57]. Moreover, the sharp peak of the relaxation rate in the vicinity of T_E is observed in μSR experiments with RB_{12} dodecaborides ($R = Er, Yb, Lu$) and $Lu_{1-x}Yb_xB_{12}$ solid solutions [58,59]. The authors [58, 59] suggested that the large amplitude dynamic features in the μSR spectra are induced by the atomic motions within the B_{12} clusters.

Below $T^* \sim 60$ K in the cage-glass state of LuB_{12} [40] the step-like Δ_{step} component appears additionally to the Δ_{smooth} contribution (see Fig. 9c, 9e) and the amplitudes of these two terms increase simultaneously with the temperature lowering. At $T=4.2$ K these anomalous positive components are not observed in low magnetic fields $H \leq 10$ kOe, and the only Δ_{smooth} contribution is detected on the angular dependences of the SIHE in the range 10-30 kOe (Figs. 9d, 9f). Then, Δ_{step} feature appears above $H^*=30$ kOe, and the $\Delta_{step}(H)$ and $\Delta_{smooth}(H)$ dependences are found to be quite different. Indeed, the smooth component saturates in the fields up to 80 kOe, while the step-like one increases strongly resulting to linear increase of the total amplitude (Fig. 9f). When RRR decreases in the studied LuB_{12} crystals the additional Δ_{smooth} contribution is only observed with the linear field dependence (see curve for the sample #2 in Fig.9f).

The analysis of the temperature dependence $\rho_H^{an}/H=f(T, H_0=80 \text{ kOe})$ in the crystals #1 and #2 allows us to reveal a hyperbolic type behavior $\rho_H^{an}/H=C^*(1/T-1/T_0)$ (Fig. 9e). The similar trend has been previously detected for anomalous transverse even component of Hall voltage in strongly correlated electron systems (SCES) $CeCu_{6-x}Au_x$ [60] and $Tm_{1-x}Yb_xB_{12}$ [50]. Similar to the results for LuB_{12} (Fig. 9e) the anomalous hyperbolic component in $Tm_{1-x}Yb_xB_{12}$ appears in high enough magnetic fields at $T_E \sim 130-150$ K, then increases drastically with the temperature lowering and saturates at liquid helium temperatures [50]. In the case of $CeCu_{6-x}Au_x$ [60] the transverse even effect is found to appear just below the structural phase transition at $T_s \sim 70$ K reaching maximum values in the quantum critical point $x_c=0.1$. The findings were discussed in [60, 50] in terms of anomalous Hall voltage caused by the interaction of external magnetic field with the filamentary structure of the many-body states. It is worth also noting that in the normal

state of the HTSC in addition to the crystalline anisotropy the origin of the anomalous Hall signal is usually attributed to the appearance of stripes both on the surface and in the layers of the superconductors [18, 61]. A similar data analysis has been developed here for the configuration ($\mathbf{I}//[1-10]$, $\mathbf{n}//[110]$) of the sample #1a, and it was found that both the amplitude of SIHE and the ordinary (cosine-type) terms are much smaller in comparison with the case ($\mathbf{I}//[1-10]$, $\mathbf{n}//[001]$) (see Figs.10 and 4a). Moreover, the additional specific $\rho_H^{\text{an}}(\varphi)$ component in this configuration has several sign reversals with at least two intervals of negative values in the vicinity of the directions $\langle 111 \rangle$ (inset in Fig.10).

Fig. 11 demonstrates the decrease of both the additional Hall signal $\rho_H^{\text{an}}/H(T, H=80 \text{ kOe})$ and the field induced resistivity component $\Delta\rho(T, 80 \text{ kOe}) = \rho(T, 80 \text{ kOe}) - \rho(T, 0 \text{ kOe})$ with the temperature increase (see Fig.3a). The behavior of these anomalous contributions may be well fitted by the analytical expressions $\rho_H^{\text{an}}/H = (\rho_H^{\text{an}}/H)_0 - AT^1 \exp(-T_0/T)$ and $\Delta\rho = \Delta\rho_0 - AT^1 \exp(-T_0/T)$ with the characteristic temperatures $T_0 = 114-140 \text{ K}$ for ρ_H^{an}/H and $140-150 \text{ K}$ for $\Delta\rho$ (the fits are shown by the solid lines in Fig.11). Note, that the behavior may be discussed in terms of the formation of the fragments (chains) of the dynamic charge stripes below $T_E \sim 150 \text{ K}$, and then, the infinite cluster of the manybody states appears below $T^* \sim 60 \text{ K}$ in the cage-glass state [62].

3.6. HE and MR anisotropy for $\mathbf{I} \parallel \langle 100 \rangle$. In the previous part of the study we have focused only on the results of the charge transport measurements for the $\mathbf{I}//[110]$ configuration, and the data obtained under the sample rotation around the $\mathbf{I}//[110]$ current axis were discussed. Indeed, this configuration is the most important and useful for the analysis of the transverse ($\mathbf{I} \perp \mathbf{H}$) galvanomagnetic effects in LuB_{12} , because, from one side, the charge stripes are directed along $\langle 110 \rangle$ axes [30, 31], and, from the other, all three principal directions $\mathbf{H}//[001]$, $[1-10]$, and $[1-11]$ are testified when rotating the crystal around this axis. At the same time, it is of extreme importance to investigate other $\mathbf{H}\text{-I}$ configurations and to characterize in more details

the charge transport anisotropy induced by the filamentary structure of quantum conduction channels in this heterogeneous medium. To check it both the transverse MR and Hall resistivity have been studied here with the current direction $\mathbf{I} // \langle 100 \rangle$. Figs. 12a and 12b show the angular (at $T=4.2$ K) and temperature dependences of resistivity, respectively, measured for the sample #2 in strong magnetic field ($H=80$ kOe). It is clearly discerned from Figs.12a-b, that below $T^* \sim 60$ K the resistivity increases noticeably. Simultaneously, (i) two $\langle 110 \rangle$ directions in the (001) plane of the *fcc* LuB_{12} lattice became non-equivalent and (ii) the $\rho(\varphi)$ dependence demonstrates a set of minima and maxima separated by $\Delta\varphi \approx 22.5^\circ$. The polar plot presented in Figs.12c-d shows the variation of the angular MR dependences in magnetic field for the samples #2 and #1c of LuB_{12} , correspondingly. Usual 4-fold anisotropy of transverse MR is detected for sample #2 in the low magnetic fields $H \leq 40$ kOe when the current is applied along the cube edge in the *fcc* lattice (Fig.12c). In higher magnetic fields the symmetry lowers dramatically when two $\langle 110 \rangle$ face diagonals become quite different. On the contrary, the 4-fold symmetry for the crystal #1c is found to break already for $H \geq 20$ kOe (Fig.12d), so that two cubic edges [100] and [001] are happened to be non-equivalent. It is seen from Fig.13a that the dramatic symmetry breaking is developed in the sample #1c in the cage-glass state of LuB_{12} (below $T^* \sim 60$ K), so that 16 equidistant directions of magnetic field corresponding to the local maxima of transverse MR are detected in the sample.

It is also worth noting, that two [010]- and [001]-elongated bars of LuB_{12} with equivalent (100), (010) and (001) faces were cut from one ingot in our previous study [29] (see, e.g., samples #1b and #1c in the inset in Fig.14a). At liquid helium temperatures their MR were found to be strongly anisotropic, demonstrating similar resistivity oscillations with the well-defined maxima separated by the period of $\Delta\varphi \approx 22.5^\circ$ (Figs. 12a, 13a). We have also compared two sets of Hall effect data for cognate crystals #1b and #1c (Fig. 14) where the z axis is the same for both samples and magnetic field is applied transverse to the stripes ($\mathbf{H} // \mathbf{n} // [001]$). As a result, the reduced Hall resistivity in both crystals demonstrates similar anomalies in the wide

neighborhood of the $\langle 001 \rangle$ direction. Note also that angular oscillations are also observed on the reduced Hall resistivity in addition to the main feature in the $\rho_H^{\text{an}}/H=f(\varphi, H=80 \text{ kOe})$ curve, they being the most noticeable for the sample #1c (see the ρ_H^{an}/H data in Fig.14b).

4. Discussion.

4.1. Fermi surface (FS) effects. At low temperatures the scattering of charge carriers in pure metals is sensitive to the topology of the Fermi surface (FS). Both quantum oscillations (de Haas-van Alphen (dHvA)/Shubnikov-de Haas (SdH) effects) and specific anomalies on the angular dependences of magnetoresistance and Hall resistivity are observed in the metals with open and closed electron orbits in high magnetic fields if $\omega_c \tau \gg 1$ (ω_c is the cyclotron frequency and τ is relaxation time) [56, 63-64]. In LuB_{12} the dHvA signal has been measured at 0.35 K for all field directions within the (010) and (011) planes in the field range 9-12 T [38], but SdH oscillations at the same temperature have been found only for one combination of $\mathbf{I}/[110]$ and $\mathbf{H}/[001]$ [38]. In our measurements at $T=4.2 \text{ K}$ weak quantum oscillations have been also detected in magnetoresistance and Hall resistivity above 10 T under the same conditions ($\mathbf{I}/[110]$ and $\mathbf{H}/[001]$, see [54] for more detail). Note that both dHvA [65] and SdH oscillations depress totally when temperature increases over 10 K. So, even if the rough estimation of $\omega_c \tau$ ($\approx \mu_H H$) in the purest crystals of LuB_{12} results in $\omega_c \tau < 1$ in magnetic fields below 12 T (see data for sample #1 in Fig. 4c) the anisotropy of the electron transport which could be induced by FS topology should be properly treated. Besides, the straightforward estimation of the concentration of conduction electron from high-temperature Hall constant $R_{H0} \approx -4 \cdot 10^{-4} \text{ cm}^3/\text{C}$ (Fig.3) results in $n_0 \approx 1.56 \cdot 10^{22} \text{ cm}^{-3}$. The value in this metal with one conduction electron per formula unit [36-39] is considerably higher than the concentration of Lu ions ($n_{\text{Lu}} = 4/a^3 \approx 0.96 \cdot 10^{22} \text{ cm}^{-3}$, $a \approx 0.746 \text{ nm}$ is the lattice parameter [29-31,66]). This means that at least two groups of charge carriers (electrons and holes) with different effective concentrations and mobilities contribute effectively to charge transport in this non-magnetic metal at room and low temperatures.

This suggestion is supported by the FS structure of LuB₁₂ that consists from one hole and two electron sheets [38,39,65,67]. This “monster” in the LuB₁₂ lower conduction band [75] (see also [54]) is very similar to that one of the noble metals (Cu, Au and Ag) if allow for the hole-electron asymmetry of the related FS sheets [38]. Indeed, similar to copper the hole-like *open orbits* in LuB₁₂ are located close to <001>, <110> and <111> [56,63,64,68] while the nearest vicinity of all these axes provides only the *closed FS sections* for $\mathbf{H} // \langle 001 \rangle$, $\mathbf{H} // \langle 110 \rangle$ and $\mathbf{H} // \langle 111 \rangle$ (see [56,63,68] for more details). This feature results in the anisotropic MR behavior with twin peak structure around $\mathbf{H} // [001]$ and $\mathbf{H} // [110]$ and the saturation of $\rho/\rho_0 \approx 4$ for $\mathbf{H} // [111]$, which was detected in LuB₁₂ at T=0.5 K and $\mu_0 H = 12$ T [38] (see also Fig. 5b-c) and was explained assuming several bunches of open orbits in the lower conduction band of this metal [38].

The similar topology of FSs in LuB₁₂ and Cu provides us by the explanation for the origin of the resistivity oscillations detected on the $\rho(\varphi)$ dependences for $\mathbf{I} // [010]$ (Figs. 12a, 13a). Indeed, the similar structure of the resistivity anomalies associated with the open orbits contribution was earlier detected for copper [63] (see polar plot Fig.12e). Note that the amplitude of these angular anomalies in the magnetoresistance of copper to be about 100-500 (Fig.12e) exceeds drastically this one in LuB₁₂ (~0.02-0.1, Figs. 12a-12d) due to higher quality of the Cu single crystals. Nevertheless, the similar positions of these resistivity maxima and the increase of their relative amplitude when increasing of magnetic field or/and lowering of temperature (Figs 12c-d, 13a) allow us to attribute these features to the contribution of open orbits, which appear for the particular directions of applied magnetic fields. In this approach, the peak features in magnetoresistance have to be accompanied by the minima in the Hall resistivity [56], which are transformed in the maxima under our subtraction procedure and can be clearly resolved in the angular dependences of the anomalous contribution ρ_H^{an}/H (see arrows in Fig.14b).

At the same time, we have to note the principal dissimilarity in the MR behavior for copper and lutetium dodecaboride. In high quality crystals of copper the FS topology results in

the MR saturation for all the principal directions of applied magnetic field (see deep minima in Fig. 5d), the unsaturated MR growth due to open orbits being detected close to all these axes. In LuB₁₂ the trend to $\rho(H)$ saturation is observed for $\mathbf{H}//[110]$ and $\mathbf{H}//[111]$ only while MR does not saturate in the wide vicinity of $\mathbf{H}//[001]$ (see Figs. 4b, 5a-5b and [38]). Note also, that the strongest MR increase in Cu is observed when $\mathbf{I}//[110]$ and magnetic field is applied along the necks of the monster ($\mathbf{H}/\langle 111 \rangle$) [54, 75]. Moreover, the MR anomaly at $\mathbf{H}//[001]$ appears in LuB₁₂ at high temperatures (below $T_E \sim 150$ K, see Figs. 11) even for the crystals with smaller mobilities (Fig. 5c and [54]). Finally, the position and the width of the MR anomaly in LuB₁₂ at $\mathbf{H}//[001]$ are just identical to those ones of the extra specific contribution to Hall effect, which was extracted as ρ_H^{an}/H in our study (see sections 3.5-3.6 and Fig.11).

In searching for the mechanism responsible for the appearance of the anomaly in MR and HE at $\mathbf{H}//[001]$ note that the SdH quantum oscillations (see Fig.4 and [54]) were measured for $\mathbf{H}//[001]$ at liquid helium temperatures in magnetic field $\mu_0 H > 10$ T in this metal with small enough average mobility of charge carriers (see $\omega_c \tau$ for sample #1 in Fig. 4c). This means that there is at least one group of carriers, for which the high-field limit $\omega_c \tau \gg 1$ is valid. According to [38], the quantum SdH oscillations for $\mathbf{H}//[001]$ are contributed from the hole-like orbits in the lower conduction band of LuB₁₂. This R₁₀₀ orbit (“four cornered rosette” [75]) corresponds to the particular dHvA α_2 branch with the extreme area $S_{\alpha_2} \approx 25$ nm² [38]. If suggest that these hole-like regions are deformed spheroids in the W points of the Brillouine zone [38] one can estimate the effective parameters of these charge carriers. In particular, leaving for the geometrical factor $G = V_{\alpha_2}/S_{\alpha_2}^{3/2} = 0.9$ (V_{α_2} and S_{α_2} – the volume and the extreme area of the FS sheet) to be intermediate between $G=1$ for cuboid and $G=4/(3\pi^{1/2}) \approx 0.75$ for spheroid, the volume of the FS sheet can be estimated as $V_{\alpha_2} = 0.9 S_{\alpha_2}^{3/2} \approx 113$ nm³, which corresponds to the $n_{\alpha_2} \approx 2.7 \cdot 10^{21}$ cm⁻³ and the effective Hall constant $R_H^{\alpha_2} = (|e| n_{\alpha_2})^{-1} \approx +2.3 \cdot 10^{-3}$ cm³/C. The condition $R_H^{\alpha_2} (\sigma_{\alpha_2})^2 \sim R_{H0} (\sigma_0)^2$ results in the conductivity ratio $\sigma_{\alpha_2}/\sigma_0 \approx 0.42$ (σ_{α_2} and σ_0 are the hole conductivity and the average conductivity, respectively). The corresponding mobility ratio is estimated as

$\mu_{\alpha 2}/\mu^*=(\sigma_{\alpha 2}n_0)/(\sigma_0n_{\alpha 2})\approx 2.4$ resulting in the value of $\mu_{\alpha 2}\approx 7100\text{ cm}^2\text{V}^{-1}\text{s}^{-1}$. Thus, for these hole-like orbits the high-field limit $\omega_c\tau\sim\mu_{\alpha 2}H_0\sim 2\pi$ gives the reasonable value for $\mu_0H_0\sim 9\text{ T}$ that agrees very well with the onset of SdH oscillations on the $\rho(H)$ and $\rho_H(H)$ data for $\mathbf{H}//[001]$ (Fig.4 and [54]). The estimation of relaxation time results in the value of $\tau=\mu_{\alpha 2}m^*_{\alpha 2}/|e|\approx 2\text{ ps}$ if allow for the effective mass value $m^*_{\alpha 2}\approx 0.53m_0$ [38]. The corresponding Dingle temperature $T_D\approx 0.6\text{ K}$ and the high enough value of related parameter $\mu_0H\tau\approx 16\text{ T}\cdot\text{ps}$ [65] prove these quantum oscillations to be observable at liquid helium temperatures.

The above speculations allow to suggest that the wide anomaly detected at $\mathbf{H}//[001]$ in the angular dependences of MR and Hall resistivity may be induced by a strong relaxation time anisotropy rather than by any specific contribution of the open orbits on the LuB_{12} FS, which seem to produce only narrow anomalies on the MR data in available magnetic fields (see Fig.5b-5c and [38]). The anisotropy of scattering time is more pronouncing in Hall effect data where noticeable deviations from cosine behavior are well resolved below 150 K (Fig.9c,e). It should be noted here that these temperatures are comparable to the vibrational energies of the rare earth ions (scaled by Einstein temperature $T_E\approx 150\text{K}$) so as strong electron-phonon interaction has to smear out any FS induced features. In this respect, any consistent model allowing for scattering time anisotropy should comprise the microscopic mechanisms, which are responsible for the formation of these “hot” and “cold” regions of FS, and the related factors, which prevent any effective mixing of these different electron states.

4.2. Stripe induced Hall effect (SIHE). The above consideration shows that any model based exclusively on the particular FS topology is insufficient to explain not only the origin of the MR anomaly for $\mathbf{H}//[100]$ and $\mathbf{I}//[011]$ (Figs. 5b-c, 6b), but also the extremely narrow step-like feature Δ_{step} and a wide range Δ_{smooth} component detected in the angular dependences of Hall resistivity at $\mathbf{H}//[001]$ for all directions of applied current (Figs.7, 9, 14b). Indeed, the wide MR anomaly at $\mathbf{H}//[001]$ is observed even for the crystals of LuB_{12} with a small enough mobility

(Fig. 5c and [54]) and at high temperatures up to 150 K (Fig. 11). It should be point out that the step-like feature in Hall resistivity at $\mathbf{H}//[001]$ is detected only for one particular combination of $\mathbf{H}//[100]$ and $\mathbf{I}//[011]$ in the highest quality crystals of LuB_{12} at temperatures up to $T^* \sim 60\text{K}$ (see Fig.9c). In this respect we note that the effects of symmetry lowering were previously established in the MR study of LuB_{12} (Fig.12-13) as the unique features of the RE dodecaboride with the dynamic charge stripes. Indeed, the corresponding electron density (ED) distribution in the LuB_{12} crystals, which was deduced from the analysis of the x-ray diffraction data with the help of the maximal entropy method (MEM) [30], is strongly inhomogeneous (Fig.13b). Assuming that pinning of the dynamic charge stripes on the randomly arranged defects and impurities fixes the selected direction in the dodecaboride matrix (Fig.13b), it is naturally to associate the *fcc* symmetry breaking with the nano-scale phase separation effects and emerging filamentary structure of conduction channels in the LuB_{12} matrix.

Note here that the discussed anomalies found in the angular dependences of magnetoresistance and Hall resistivity are specific for both magnetic and nonmagnetic $\text{Ho}_x\text{Lu}_{1-x}\text{B}_{12}$ compounds [70, 71]. These common features increase strongly below $T^* \sim 60\text{ K}$ (see Fig.11) in the cage-glass state [40, 29]. In our opinion, these similarities favor to the explanation for the significant MR increase in the vicinity of $\mathbf{H}//[001]$, which has been proposed recently in [70, 72]. We consider the strong interaction of the dynamic stripes along the [110] direction with the transverse external magnetic field (Fig.1a) as the possible reason for the detected increase of the amplitude of the negative cosine-type component (absolute values of the ordinary Hall effect), which is clearly observed with increase of external magnetic field (Fig. 4a). This behavior (see Figs. 7-8 and Figs.S4,S5 in [54]) is accompanied by the changes of the average mobility in the LuB_{12} crystals. The measurements of optical conductivity in LuB_{12} [35] revealed that the conduction band consists of (i) Drude electrons and (ii) non-equilibrium (hot) charge carriers involved in the collective modes and seen in the conductivity spectra as overdamped oscillators. As non-equilibrium electrons amount about $\sim 70\%$ of the total electron concentration, the related

approach should include some redistribution of electrons between these two electron sub-systems. A rough estimation obtained from the optical conductivity spectra [67] proves that the relative number of the Drude-type and hot charge carriers does not change in LuB_{12} at low temperatures. We suggest that strong impurity scattering provokes fast thermalization of the hot electrons, but, on the contrary, strong external magnetic field increases the number of electrons in these dynamic charge stripes. As a result, both the impurity concentration and external magnetic field may be considered as two factors, which are responsible for the redistribution of charge carriers between the non-equilibrium and Drude-type electron sub-systems in the heterogeneous medium of LuB_{12} non-magnetic metal with dynamic charge stripes.

This redistribution may also increase the amplitude of the Hall effect component, which is induced by the stripes (SIHE). In this scenario the low temperature enhancement of the negative ordinary Hall coefficient (marked as cos in Fig. 4a) observed in strong magnetic field should be attributed to the decrease of free electron concentration n_e . The n_e evolution is accompanied with a dramatic increase of the SIHE amplitude (Figs. 9d, 9f, 11 and 14). In this picture the field-induced decrease of a number of carriers $\Delta n_e/n_e$ in the LuB_{12} matrix is dependent on the direction of external magnetic field. The effect is happened to reach the largest value ($\sim 30\%$) for \mathbf{H} to be transverse to dynamic charge stripes ($\mathbf{H} // \mathbf{n} // [001]$, see schema in Fig. 1a), while only relatively small ($\sim 10\%$) changes are observed for $\mathbf{H} // [110]$ (Fig. 4a). The validity of the SIHE scenario could be verified in future both by precise magnetotransport study and optical measurements in high magnetic field. Note here only that the redistribution in magnetic field of the charge carriers between the Drude-type and hot, non-equilibrium electron sub-systems may be attributed to the reasons of emergence of anomalous Hall effect in the dodecaborides with magnetic RE ions, e.g., such as $\text{Ho}_x\text{Lu}_{1-x}\text{B}_{12}$ [76].

5. Conclusion.

Summarizing the specific features of magnetoresistance and Hall resistivity found in the present study for the non-magnetic metal LuB_{12} with dynamic electron stripes, we outline the different factors, which may result in the anomalies of electron transport in this material. While some peculiarities found in the angular dependences of MR (16 maxima for $I//[001]$ and twin peak fine structure around $\mathbf{H}//[001]$ and $\mathbf{H}//[1-10]$ for $I//[110]$) and Hall resistivity may be definitely associated with the presence of open orbits in the corresponding sections of FS, the origin of the wide feature at $H//[001]$ found both in MR and HE requires further theoretical consideration. The estimations based on the FS topology show that this anomaly could appear due to the relevant contribution of the holes with large enough mobility ($7100 \text{ cm}^2\text{V}^{-1}\text{s}^{-1}$) and relaxation time (2 ps), but these parameters decrease dramatically at high temperatures (up to 150 K) prohibiting this kind scenario. In contrary, the inhomogeneous distribution of electron density in LuB_{12} initiated by the cooperative JT effect in the B_{12} clusters in the presence of the rattling modes of Lu ions may also result in the additional component in Hall resistivity. In the last case the configuration dependent contribution to Hall effect arises due to interaction of magnetic field with the filamentary structure of dynamic charge stripes, which pin occasionally along one of $\langle 110 \rangle$ principal directions of the *fcc* lattice. However, the approach requires a careful consideration of the processes, which determine the redistribution of the charge carriers between “cold” (Drude-like) and “hot” (non-equilibrium) channels. Indeed, the strong anisotropy of relaxation time with its low enough average value may be induced by the cooperative JT instability of the B_{12} - clusters in LuB_{12} . The related ferrodistorive effect in the boron sublattice may induce the periodic changes in the $5d-2p$ hybridization modulating the width of the conduction band and increasing the intensity of charge carrier scattering. In this scenario the related “breathing” of FS should lead to periodic changes of size for both the belly and necks of the hole-like FS monster [54] and may be considered as the main factor responsible for the average τ decrease and the depression of the SdH oscillations in LuB_{12} . In this respect the step-

like feature in Hall resistivity detected only for one combination of $\mathbf{H}//[100]$ and $\mathbf{I}//[011]$ in the high quality single crystals of LuB_{12} (see sections 3.5-3.6) may be treated as a key feature to check the validity of the theoretical approaches proposed for explanation of the magnetotransport anomalies in this compound.

Acknowledgements. This work was supported by the Russian Science Foundation, project no. 17-12-01426 (MR measurements) and Russian Foundation for Basic Research, project no. 18-02-01152 (Hall effect study). The authors are grateful to V.N. Krasnorussky for experimental assistance and useful discussions.

References.

- [1] S. Sachdev, *Rev. Mod. Phys.* **75**, 913 (2003).
- [2] P. A. Lee, N. Nagaosa, and X.-G. Wen, *Rev. Mod. Phys.* **78**, 17 (2006).
- [3] T. Timusk and B. W. Statt, *Rep. Prog. Phys.* **62**, 61 (1999).
- [4] E. W. Carlson, V. J. Emery, S. A. Kivelson, and D. Orgad, in: *The Physics of Conventional and Unconventional Superconductors*, K. H. Bennemann and J. B. Ketterson, eds. (Springer, 2003).
- [5] M. R. Norman, D. Pines, and C. Kallin, *Adv. Phys.* **54**, 715 (2005).
- [6] P. A. Lee, *Rep. Prog. Phys.* **71**, 012501 (2008).
- [7] J. Zaanen, *Physica C* **317**, 217 (1999).
- [8] S. A. Kivelson, I. P. Bindloss, E. Fradkin, V. Oganesyan, J. M. Tranquada, A. Kapitulnik, and C. Howald, *Rev. Mod. Phys.* **75**, 1201 (2003).
- [9] A. Damascelli, Z. Hussain, and Z. X. Shen, *Rev. Mod. Phys.* **75**, 473 (2003).
- [10] T. Yoshida *et al.*, *J. Phys.: Cond. Matter* **19**, 125209 (2007).
- [11] Ø. Fischer, M. Kugler, I. Maggio-Aprile, C. Berthod, and C. Renner, *Rev. Mod. Phys.* **79**, 353 (2007).
- [12] E. Demler, W. Hanke, and S.-C. Zhang, *Rev. Mod. Phys.* **76**, 909 (2004).
- [13] M. Ogata and H. Fukuyama, *Rep. Prog. Phys.* **71**, 036501 (2008).
- [14] M. Vojta, *Adv. Phys.* **58**, 699 (2009).
- [15] J. M. Tranquada, B. J. Sternlieb, J. D. Axe, Y. Nakamura, and S. Uchida, *Nature* **375**, 561 (1995).

- [16] C. Stock et al., Phys. Rev. B **69**, 014502 (2004).
- [17] H.A. Mook, P. Dai, F. Dogan and R.D.Hunt, Nature (London) **404**, 729 (2000).
- [18] M. R. Koblischka, M. Winter and U. Hartmann, Supercond. Sci. Technol. **20**, 681(2007)
- [19] Y. Kohsaka, C. Taylor, K. Fujita, A. Schmidt, C. Lupien, et al., Science **315**,1380 (2007);
E. H. da Silva Neto, P. Aynajian, A. Frano, R. Comin, E. Schierle, E. Weschke, A. Gyenis, J. Wen, J. Schneeloch, Z. Xu, S. Ono, G. Gu, M. Le Tacon, A. Yazdani, Science **343**, 393 (2014)
- [20] T. Hanaguri, C. Lupien, Y. Kohsaka, D.H. Lee, M. Azuma, et al., Nature **430**, 1001 (2004)
- [21] S. Mori, C. H. Chen, and S.-W. Cheong, Nature **392**, 473 (1998).
- [22] M. Rubhausen, S. Yoon, S.L. Cooper, K.H. Kim, S.W. Cheong, Phys. Rev. B **62**, R4782 (2000)
- [23] S.-H. Lee and S-W. Cheong, Phys. Rev. Lett. **79**, 2514 (1997).
- [24] J. M. Tranquada, J. Phys. Chem. Solids **59**, 2150 (1998).
- [25] A. M. M. Abeykoon et.al., Phys. Rev. Lett. **111**, 096404 (2013)
- [26] Qisi Wang, Yao Shen, Bingying Pan, Yiqing Hao, Mingwei Ma, Fang Zhou, P. Steens, K. Schmalzl, T. R. Forrest, M. Abdel-Hafiez, Xiaojia Chen, D. A. Chareev, A. N. Vasiliev, P. Bourges, Y. Sidis, Huibo Cao and Jun Zhao, Nature Materials **15**, 159 (2016)
- [27] R. M. Fernandes, A. V. Chubukov, J. Schmalian, Nature Physics **10**, 97 (2014)
- [28] S. V. Demishev, V. N. Krasnorussky, A. V. Bogach, V. V. Voronov, N. Yu. Shitsevalova, V. B. Filipov, V. V. Glushkov, N. E. Sluchanko, Scientific Reports **7**, 17430 (2017)
- [29] N. Sluchanko, A. Bogach, N. Bolotina, V. Glushkov, S. Demishev, A. Dudka, V. Krasnorussky, O. Khrykina, K. Krasikov, V. Mironov, V. B. Filipov, and N. Shitsevalova,

Rattling mode and symmetry lowering resulting from the instability of the B-12 molecule in LuB_{12} , *Phys. Rev. B* **97**, 035150 (2018).

[30] N. B. Bolotina, A. P. Dudka, O. N. Khrykina, V. N. Krasnorussky, N. Y. Shitsevalova, V. B. Filipov, and N. E. Sluchanko, The lower symmetry electron-density distribution and the charge transport anisotropy in cubic dodecaboride LuB_{12} , *J. Phys.: Condens. Matter* **30**, 265402 (2018).

[31] N. B. Bolotina, A. P. Dudka, O. N. Khrykina, V. V. Glushkov, A. N. Azarevich, V. N. Krasnorussky, S. Gabani, N. Y. Shitsevalova, A. V. Dukhnenko, V. B. Filipov, and N. E. Sluchanko, On the role of isotopic composition in crystal structure, thermal and charge-transport characteristics of dodecaborides (Lu^NB_{12}) with the Jahn-Teller instability, *J. Phys. Chem. Solids* **129**, 434 (2019).

[32] N. E. Sluchanko, A. N. Azarevich, A. V. Bogach, N. B. Bolotina, V. V. Glushkov, S. V. Demishev, A. P. Dudka, O. N. Khrykina, V. B. Filipov, N. Y. Shitsevalova, G. A. Komandin, A. V. Muratov, Y. A. Aleshchenko, E. S. Zhukova, and B. P. Gorshunov, Observation of dynamic charge stripes in $\text{Tm}_{0.19}\text{Yb}_{0.81}\text{B}_{12}$ at the metal-insulator transition, *J. Phys.: Condens. Matter* **31**, 065604 (2019).

[33] I. Bersuker, *The Jahn-Teller Effect* (Cambridge University Press, Cambridge, 2006).

[34] A. V. Rybina, K. S. Nemkovski, P. A. Alekseev, J. M. Mignot, E. S. Clementyev, M. Johnson, L. Capogna, A. V. Dukhnenko, A. B. Lyashenko, and V. B. Filippov, Lattice dynamics in ZrB_{12} and LuB_{12} : Ab initio calculations and inelastic neutron scattering measurements, *Phys. Rev. B* **82**, 024302 (2010).

[35] B. P. Gorshunov, E. S. Zhukova, G. A. Komandin, V. I. Torgashev, A. V. Muratov, Y. A. Aleshchenko, S. V. Demishev, N. Y. Shitsevalova, V. B. Filipov, and N. E. Sluchanko, Collective Infrared Excitation in LuB_{12} Cage-Glass, *JETP Lett.* **107**, 100 (2018).

- [36] H. Harima, A. Yanase, and T. Kasuya, Energy band structure of YB_{12} and LuB_{12} , *J. Magn. Magn. Mater.* **47**, 567 (1985).
- [37] H. Harima, N. Kobayashi, K. Takegahara, and T. Kasuya, Band calculations with occupied 4f electrons, *J. Magn. Magn. Mater.* **52**, 367 (1985).
- [38] M. Heinecke, K. Winzer, J. Noffke, H. Kranefeld, H. Grieb, K. Flachbart, and Y. B. Paderno, Quantum oscillations and the Fermi surface of LuB_{12} , *Zeitschrift für Physik B: Condensed Matter* **98**, 231 (1995).
- [39] G. E. Grechnev, A. E. Baranovskiy, V. D. Fil, T. V. Ignatova, I. G. Kolobov, A. V. Logosha, N. Y. Shitsevalova, V. B. Filippov, and O. Eriksson, Electronic structure and bulk properties of MB_6 and MB_{12} borides, *Low Temp. Phys.* **34**, 921 (2008).
- [40] N. E. Sluchanko, A. N. Azarevich, A. V. Bogach, I. I. Vlasov, V. V. Glushkov, S. V. Demishev, A. A. Maksimov, I. I. Tartakovskii, E. V. Filatov, K. Flachbart, S. Gabani, V. B. Filippov, N. Y. Shitsevalova, and V. V. Moshchalkov, Effects of disorder and isotopic substitution in the specific heat and Raman scattering in LuB_{12} , *JETP* **113**, 468 (2011).
- [41] P. Coleman, C. Pepin, Q. Si, and R. Ramazashvili, *J. Phys. Cond. Mat.* **13**, R723(2001).
- [42] P. Coleman, J. B. Marston, and A. J. Schofield, *Phys. Rev. B* **72**, 245111 (2005).
- [43] S. Paschen, T. Luhmann, S. Wirth, et al., *Nature* **432**, 881 (2004).
- [44] A. Yeh, Yeong-Ah Soh, J. Brooke, et al., *Nature* **419**, 459 (2002).
- [45] Jie Lin and A. J. Millis, Theory of low-temperature Hall effect in stripe-ordered cuprates: Relative phase of the charge and spin potentials, *Phys. Rev. B* **80**, 193107(2009).
- [46] L. Xie, J F Ding, R. R. Guo, X. F. Sun and X. G. Li <https://iopscience.iop.org/journal/0953-8984> Interplay between charge stripes and sign reversals of Hall and Seebeck effects in stripe-ordered $\text{La}_{1.6-x}\text{Nd}_{0.4}\text{Sr}_x\text{CuO}_4$ superconductors, *J. Phys.: Condens. Matter* **23**, 365702 (2011).
- [47] D. W. Koon and T. G. Castner, Hall effect near the metal-insulator transition

Phys. Rev. B **41**, 12054 (1990).

[48] W. Teizer, F. Hellman, and R. C. Dynes, Hall effect at a tunable metal-insulator transition

Phys. Rev. B **67**, 121102 (2003).

[49] Fangdong Tang, Yafei Ren, Peipei Wang, Ruidan Zhong, John Schneeloch, Shengyuan A.

Yang, Kun Yang, Patrick A. Lee, Genda Gu, Zhenhua Qiao & Liyuan Zhang, Three-dimensional quantum Hall effect and metal–insulator transition in ZrTe_5 Nature **569**, 537–541(2019).

[50] N. E. Sluchanko, A. N. Azarevich, A. V. Bogach, V. V. Glushkov, S. V. Demishev, M. A.

Anisimov, A. V. Levchenko, V. B. Filipov, and N. Y. Shitsevalova, Hall and transverse even effects in the vicinity of a quantum critical point in $\text{Tm}_{1-x}\text{Yb}_x\text{B}_{12}$, JETP **115**, 509 (2012).

[51] K. Hagiwara, Y. Takeno, Y. Ohtsubo, R. Yukawa, M. Kobayashi, K. Horiba, H.

Kumigashira, J. Rault, P. Le Fèvre, and F. Bertran, J. Phys.: Conf. Ser. **807**, 012003 (2017).

[52] A. Rousuli, H. Sato, F. Iga, K. Hayashi, K. Ishii, T. Wada, T. Nagasaki, K. Mimura, H.

Anzai, K. Ichiki, S. Ueda, A. Kondo, K. Kindo, T. Takabatake, K. Shimada, H. Namatame, and M. Taniguchi, Hard x-ray photoemission study of $\text{Yb}_{1-x}\text{Zr}_x\text{B}_{12}$: the effects of electron doping on the Kondo insulator YbB_{12} , J. Phys. Cond. Mat. **29**, 265601 (2017).

[53] H. Werheit, V. Filipov, K. Shirai, H. Dekura, N. Shitsevalova, U. Schwarz, M. Armbruster,

Raman scattering and isotopic phonon effects in dodecaborides, J. Phys.: Cond. Matter. **23**

065403 (2011). <http://iopscience.iop.org/article/10.1088/0953-8984/23/6/065403/meta>

[54] Supplemental Material at <http://link.aps.org/supplemental/>: the details of the LuB_{12} crystal

growth; comparison of the amplitude of the resistivity and the Hall resistivity anomalies on the angular dependences (**Fig.S1**); magnetic field dependences of the reduced Hall resistivity ρ_H/H ,

resistivity and Hall mobility in LuB_{12} for the samples #2 and #3 (**Figs.S2-S3**); liquid helium

angular dependences of resistivity in the sample #5 of LuB_{12} (**Fig.S4**); the comparison of the

reduced Hall resistivity angular dependences for the samples #1, #2 and #3 of LuB_{12} (**Figs.S5-**

S6), the separation of the ordinary (cosin-type) and anomalous components in the reduced Hall

resistivity for the sample #2 of LuB₁₂ (**Figs.S7-S8**); the hole-type Fermi surface sheet in LuB₁₂ (**Fig.S9**); quantum oscillations of resistivity and the reduced Hall resistivity in LuB₁₂ (sample #1a) (**Fig.S10**).

[55] A. Anselm, Introduction to semiconductor theory, English translation, Mir Publishers, Moscow, 1981.

[56] I. M. Lifshits, M. Ya. Azbel, and M. I. Kaganov, *Electron Theory of Metals* (Consultants Bureau, New York, 1973)]

[57] D. Parshin, Model of soft potentials and universal properties of glasses, *Phys. Solid State* **36**, 991 (1994).

[58] G. M. Kalvius, D. R. Noakes, R. Wappling, A. Kratzer, E. Schreier, F. Iga, T. Takabatake, and H. Von Lohneysen, muSR spectroscopy of the Kondo insulators Lu_{1-x}Yb_xB₁₂, *Physica B* **312**, 210 (2002).

[59] G. M. Kalvius, D. R. Noakes, N. Marcano, R. Wappling, F. Iga, and T. Takabatake, Dynamics of the internal field in RB₁₂ (R = Er, Yb, Lu), *Physica B* **326**, 398 (2003).

[60] N. E. Sluchanko, D. N. Sluchanko, N. A. Samarin, V. V. Glushkov, S. V. Demishev, A. V. Kuznetsov, G. S. Burkhanov, and O. D. Chistyakov, *Low Temp. Phys.* **35**, 544 (2009).

[61] I. Janecek, and P. Vašek, arXiv:cond-mat/0306560.

[62] N.E. Sluchanko, Magnetism, quantum criticality, and metal-insulator transitions in RB₁₂, arXiv:2004.06371

[63] J. R. Klauder and J. E. Kunzler, *The Fermi Surface* (Wiley, New York, 1960).

[64] A. B. Pippard, *Magnetoresistance in Metals* (Cambridge University Press, New York, 1989)

[65] Hsu Liu, M. Hartstein, G.J. Wallace, A. J. Davies, M. C. Hatnean, M. D. Johannes, N. Shitsevalova, G. Balakrishnan, S.E. Sebastian, Fermi surfaces in Kondo insulators, *J. Phys.: Condens. Matter* **30** (2018) 16LT01 <https://doi.org/10.1088/1361-648X/aaa522>

- [66] H. Hein, C. Koeppel, U. Vetter, E. Warkentin, Sc, Y, La-Lu. Rare Earth Elements: Compounds with Boron, Springer Science & Business Media, 2013, p.103.
- [67] J. Teyssier, R. Lortz, A. Petrovic, D. Van Der Marel, V. Filippov, N. Shitsevalova, Effect of electron-phonon coupling on the superconducting transition temperature in dodecaboride superconductors: A comparison of LuB_{12} with ZrB_{12} , *Phys. Rev. B* **78**, 134504 (2008).
- [68] I. M. Lifshits, V. G. Peschanski, *Sov. Phys. JETP* **11**, 137 (1960).
- [69] Sheng Nan Zhang, Quan Sheng Wu, Yi Liu, O.V. Yazyev, Magnetoresistance from Fermi surface topology, *Phys. Rev. B* **99**, 035142 (2019).
- [70] N. E. Sluchanko, A. L. Khoroshilov, A. V. Bogach, V. V. Voronov, V. V. Glushkov, S. V. Demishev, V. N. Krasnorussky, K. M. Krasikov, N. Yu. Shitsevalova, V. B. Filipov, MR Scaling and the Anisotropy of Charge Carrier Scattering in the Paramagnetic Phase of $\text{Ho}_{0.8}\text{Lu}_{0.2}\text{B}_{12}$ Cage Glass, *JETP Lett.* **107**, 30 (2018).
- [71] A. L. Khoroshilov, A. N. Azarevich, A. V. Bogach, V. V. Glushkov, S. V. Demishev, V. N. Krasnorussky, V. V. Voronov, N. Yu. Shitsevalova, V. B. Filippov, S. Gabani, K. Flachbart, N. E. Sluchanko, *J. Low Temp. Phys.* **185**, 522 (2016).
- [72] N. E. Sluchanko, A. L. Khoroshilov, V. N. Krasnorussky, A. V. Bogach, V. V. Glushkov, S. V. Demishev, K. M. Krasikov, N. Yu. Shitsevalova, V. B. Filippov, Magnetic Phase Transitions and the Anisotropy of Charge Carrier Scattering in Antiferromagnetic Metal $\text{Ho}_{0.5}\text{Lu}_{0.5}\text{B}_{12}$ with Dynamic Charge Stripes, *Bulletin of the Russian Academy of Sciences: Physics* **83**, 853 (2019).
- [73] A.L. Khoroshilov, V.N. Krasnorussky, K.M. Krasikov, A.V. Bogach, V.V. Glushkov, S.V. Demishev, N.A. Samarin, V.V. Voronov, N.Yu. Shitsevalova, V.B. Filipov, S. Gabáni, K. Flachbart, K. Siemensmeyer, S. Yu. Gavrilkin, N.E. Sluchanko, Maltese cross anisotropy in $\text{Ho}_{0.8}\text{Lu}_{0.2}\text{B}_{12}$ antiferromagnetic metal with dynamic charge stripes, *Phys. Rev. B* **99**, 174430 (2019). DOI: 10.1103/PhysRevB.99.174430.
- [74] A. Khoroshilov, V. Krasnorussky, A. Bogach, V. Glushkov, S. Demishev, Levchenko, N. Shitsevalova, V. Filippov, S. Gabáni, K. Flachbart, K. Siemensmeyer, N. Sluchanko,

Anisotropy of MR in HoB₁₂, Acta Physica Polonica A **131**, 976 (2017). DOI:

10.12693/APhysPolA.131.976

[75] D. Shoenberg, Magnetic oscillations in metals, Cambridge, Cambridge University Press, 1984.

[76] V. Krasnorussky, V. Glushkov, A. Bogach, S. Demishev, N. Shitsevalova, V. Filipov, G. Pristas, S. Gabani, K. Flachbart, N. Sluchanko, Anomalous Magnetic Contributions to Hall Effect in Ho_{0.5}Lu_{0.5}B₁₂, Acta Phys. Polon. A **137**, 767 (2020)

[77] J.R. Klauder, W.A. Reed, G.F. Brennert, J.E. Kunzler, Study of the Fine Structure of the High-Field Galvanomagnetic Properties and the Fermi Surface of Copper, Phys. Rev. **141**, 592 (1966).

Figure captions.

Fig.1. (a) Crystal structure of RB_{12} . Color plane shows the map of the electron density in the face (001) obtained by the maximum entropy method (MEM) [29]. Green bars correspond to the dynamic charge stripes. Directions along ($\mathbf{n}/[110]$) and transverse ($\mathbf{n}/[001]$) to the stripes are shown. (b) Fragment of the crystal structure demonstrates two connected B_{24} clusters with embedded Lu^{3+} ions. (c) The schematic view of two double-well potentials for neighboring Lu-ions.

Fig. 2. Temperature dependences of (a) the resistivity and (b) Hall mobility at $H=80$ kOe of the LuB_{12} crystals. Vertical dashed line marks the transition at $T^*\sim 60$ K to the cage-glass state.

Fig.3. Temperature dependences of resistivity for the LuB_{12} crystals #1a (panel a), #2 (c) and #3 (e), and of the reduced Hall resistivity for crystals #1a (panel b), #2 (d) and #3 (f) at $H=80$ kOe. Vertical dashed line marks the transition at $T^*\sim 60$ K to the cage-glass state. Large open symbols correspond to the ordinary Hall coefficient (marked as cos) and the sum of the ordinary and anomalous components (see text for details).

Fig.4. Magnetic field dependences of the reduced Hall resistivity (a), resistivity (b), and the Hall mobility (b) of the LuB_{12} crystal #1a at the liquid helium temperature. Large open symbols on the panel (a) correspond to the ordinary Hall coefficient (marked as cos) and the sum of the ordinary and anomalous components (see text for details).

Fig.5. Magnetic field (a) and angular (b) dependences of resistivity of the sample #1a of LuB_{12} at $T=4.2$ K. For comparison the resistivity $\rho(\varphi, T=4.2$ K, $H=80$ kOe) curves for several LuB_{12} samples are shown in panel (c). Schematic view of the sample for the galvanomagnetic measurements is presented in the insert in panel (a). Panel (d) shows the results of similar transverse MR rotations for copper ($T=4.2$ K, $H=18$ kOe, $\text{RRR}=8000$, adapted from [63]).

Fig.6. (a) The polar plot of resistivity of the sample #1a at $T=4.2$ K. (b) The presentation in the cylindrical coordinates of the temperature dependence of MR of the sample #1a at $H=80$ kOe. Color shows the MR amplitude.

Fig.7. Angular dependences of the reduced Hall resistivity ρ_H/H for the samples #1a (panel a), #2 (b) and #3 (c) at liquid helium temperature in the configuration $\mathbf{I}/[110]$, $\mathbf{n}/[001]$. Solid line in

(c) demonstrates the cosin-type approximation. Vertical arrows in (a) show two \mathbf{H} directions in the traditional, common-used technique of the Hall effect measurements.

Fig.8. Angular dependences of the reduced Hall resistivity ρ_H/H for the samples #1a (panel a), #2 (b) and #3 (c) at liquid helium temperature in the configuration $\mathbf{I}/[110]$, $\mathbf{n}/[110]$. Vertical arrows in (a) show two \mathbf{H} directions in the traditional, common-used technique of the Hall effect measurements.

Fig.9. Angular dependences of the reduced Hall resistivities ρ_H/H and ρ_H^{an}/H in the configuration $\mathbf{I}/[110]$, $\mathbf{n}/[001]$ in the sample #1a for various temperatures at $H=80$ kOe (panels a and c) and in different magnetic fields at $T=4.2$ K (panels b and d), correspondingly. Solid lines in (b) demonstrate the examples of the cosin-type approximation. Δ_{smooth} and Δ_{step} in (c) and (d) denote two anomalous components in the anomalous reduced Hall resistivity ρ_H^{an}/H . The reciprocal temperature plot in (e) shows the behavior of $\rho_H^{\text{an}}/H=f(T)$ detected in the crystals #1a and #2. Panel (f) presents the field dependence of $\rho_H^{\text{an}}/H=f(H, T=4.2 \text{ K})$ and Δ_{smooth} , Δ_{step} components. T_E and T^* are the energy scales in the LuB_{12} (see text).

Fig.10. Angular dependences of the reduced Hall resistivities ρ_H/H and ρ_H^{an}/H in the configuration $\mathbf{I}/[1-10]$, $\mathbf{n}/[110]$ in the sample #1a for various magnetic fields at $T=4.2$ K. Solid lines demonstrate the examples of the cosin-type approximation. Insert shows large scale view of $\rho_H^{\text{an}}/H=f(\varphi, H=80 \text{ kOe}, T=4.2 \text{ K})$.

Fig.11. The temperature dependences of the anomalous reduced Hall resistivity ρ_H^{an}/H and resistivity $\Delta\rho$ components for the samples #1a (a) and #2 (b). Solid lines show the analytical approximation by $(\rho_H^{\text{an}}/H, \Delta\rho) = (\rho_H^{\text{an}}/H, \Delta\rho)_0 - AT^{-1}\exp(-T_0/T)$. Vertical dashed line marks the transition at $T^*\sim 60$ K to the cage-glass state.

Fig.12. (a) Angular ($T=4.2$ K) (b) temperature dependences of resistivity of the sample #2 of LuB_{12} at $H=80$ kOe. For comparison, the polar plots (c) and (d) at $T=4.2$ K demonstrate the angular dependences of the normalized MR for the samples #2 and #1c, correspondingly). Panel (e) shows the results of similar resistivity/transverse MR rotations for copper ($T=4.2$ K, $H=18$ kOe, $\text{RRR}=8000$, adapted from [77]).

Fig.13. (a) The presentation in the polar coordinates of the temperature dependence of resistivity of the sample #1c at $H=80$ kOe ($\mathbf{I}/[010]$). Color shows the resistivity amplitude, arrows mark the

harmonics (see text). (b) The map of the electron density distribution in LuB_{12} obtained by the maximum entropy method [29].

Fig.14. Angular dependences of the reduced Hall resistivity ρ_H/H for the samples #1b (panel a, $\mathbf{I}/[100]$) and #1c (b, $\mathbf{I}/[010]$) at liquid helium temperature in the configuration $\mathbf{n}/[001]$. Solid line in (b) demonstrates the cosine-type approximation, $\rho_H^{\text{an}}/H(\varphi)$ shows the anomalous component. Arrows marks the harmonics (see text). Insert shows schematically how the samples #1b and #1c cut from the single crystalline disc of LuB_{12} .

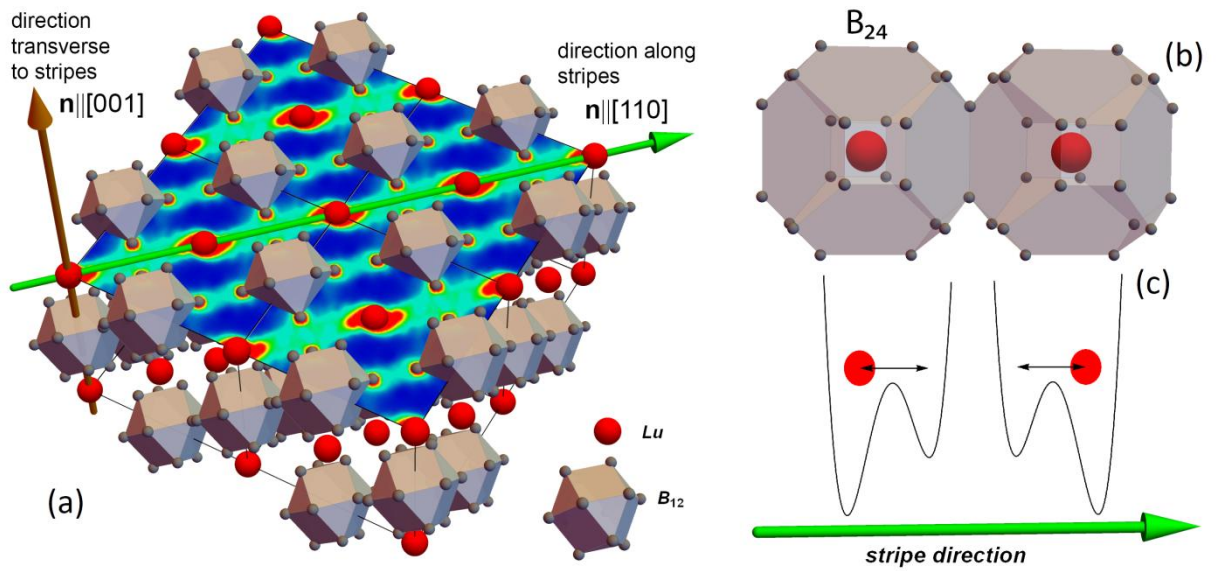


Fig. 1.

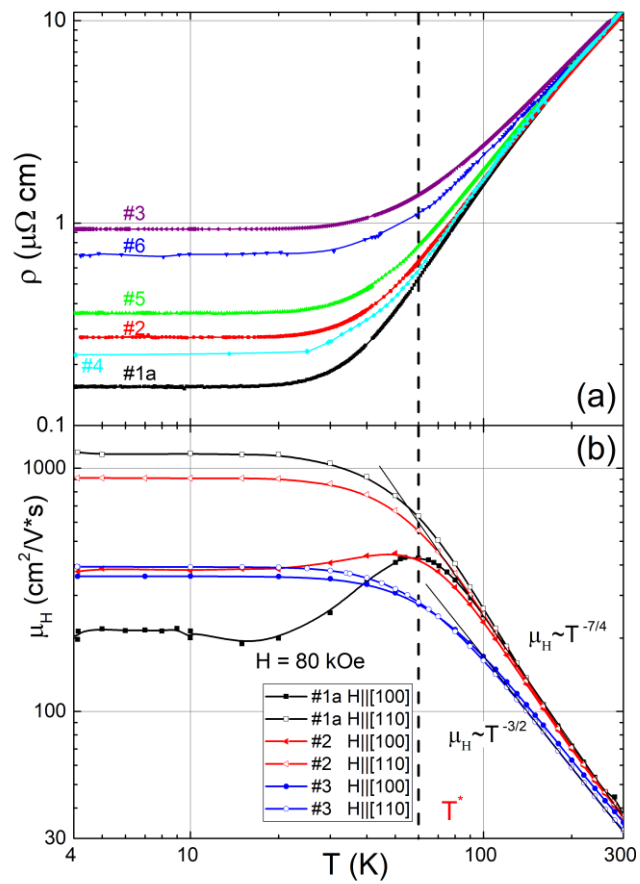


Fig. 2.

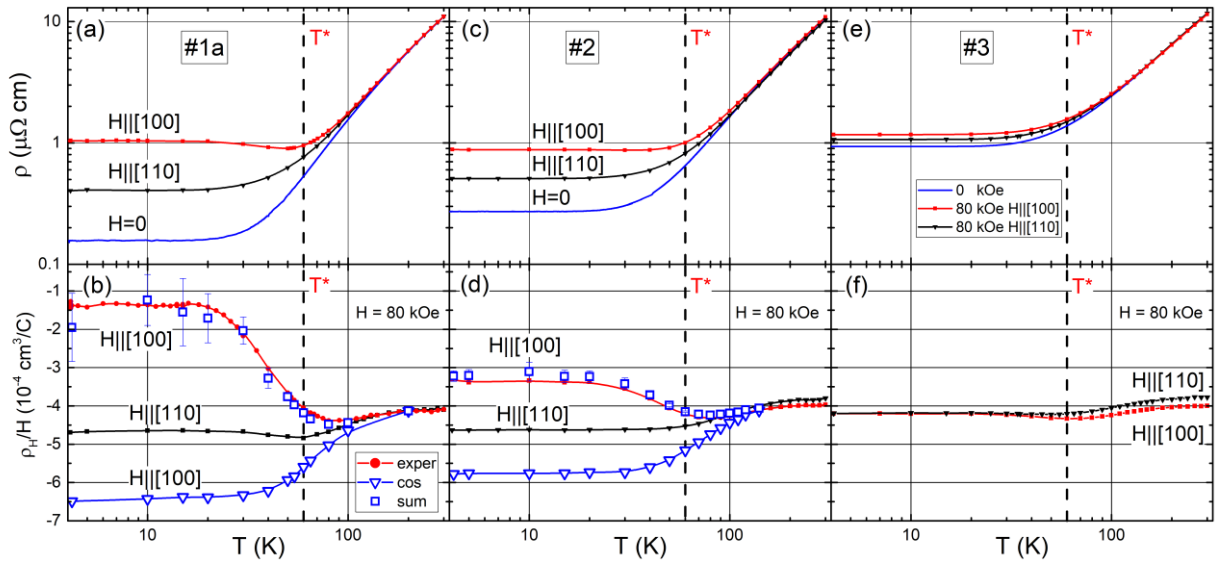


Fig.3.

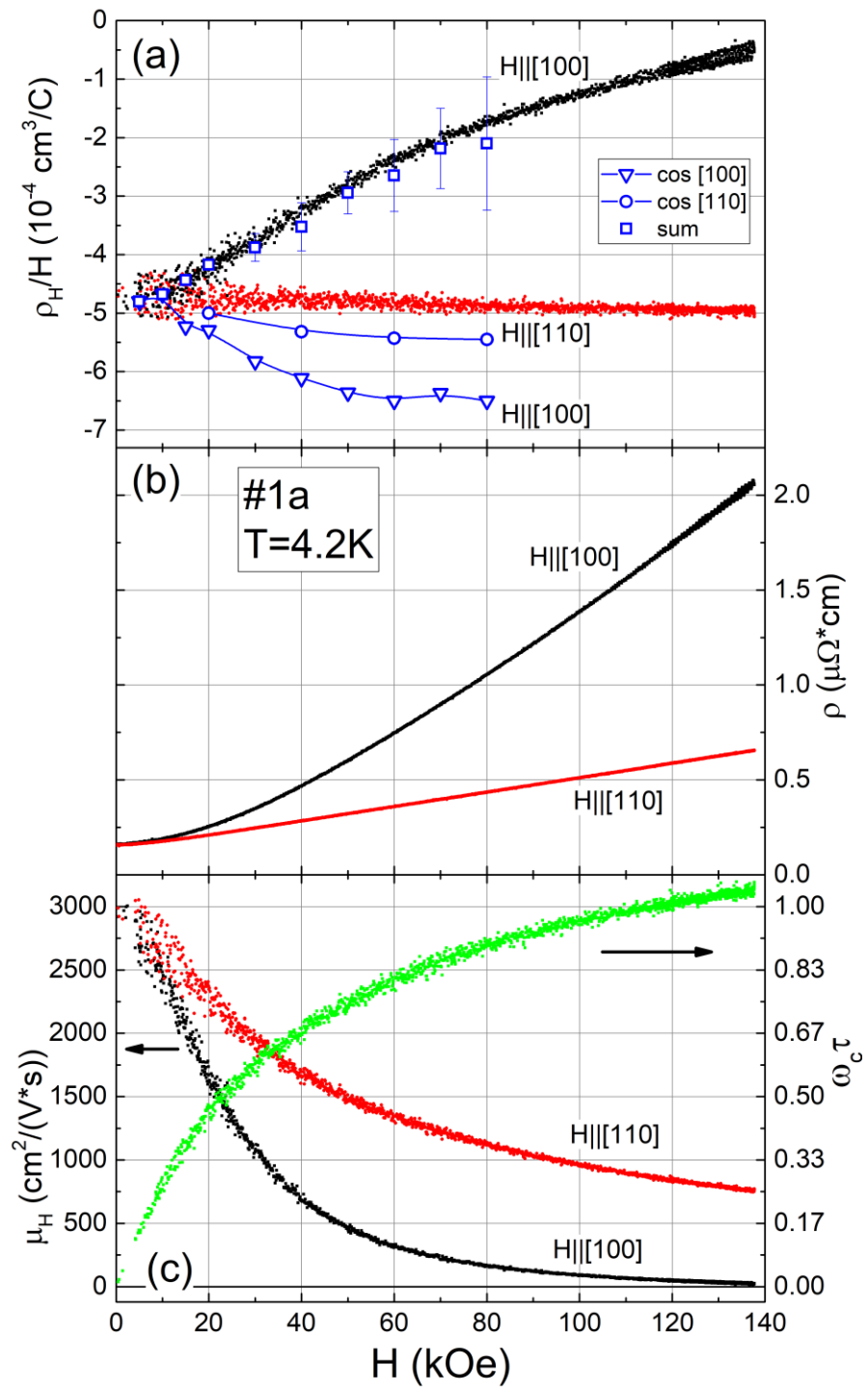


Fig.4.

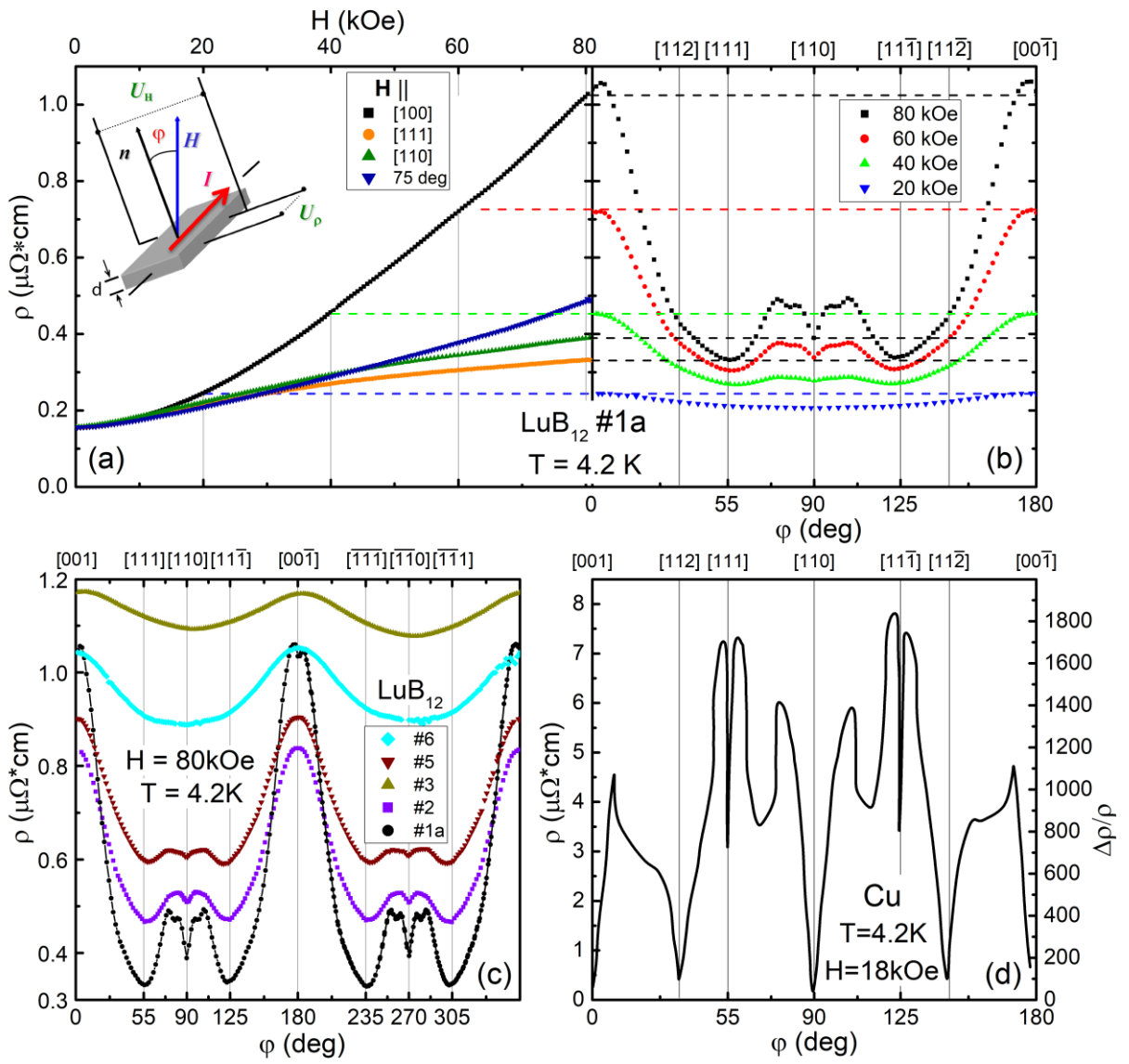


Fig.5.

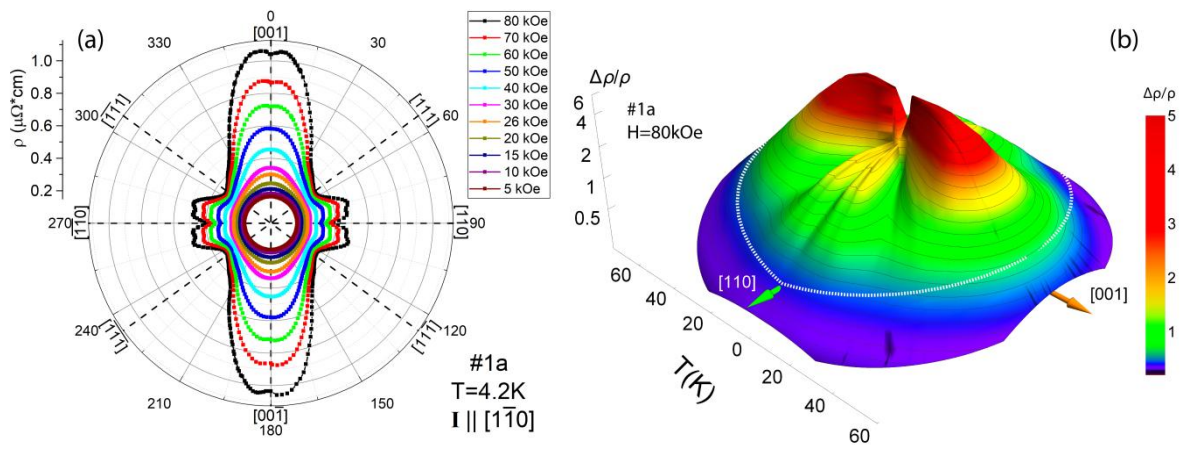


Fig.6.

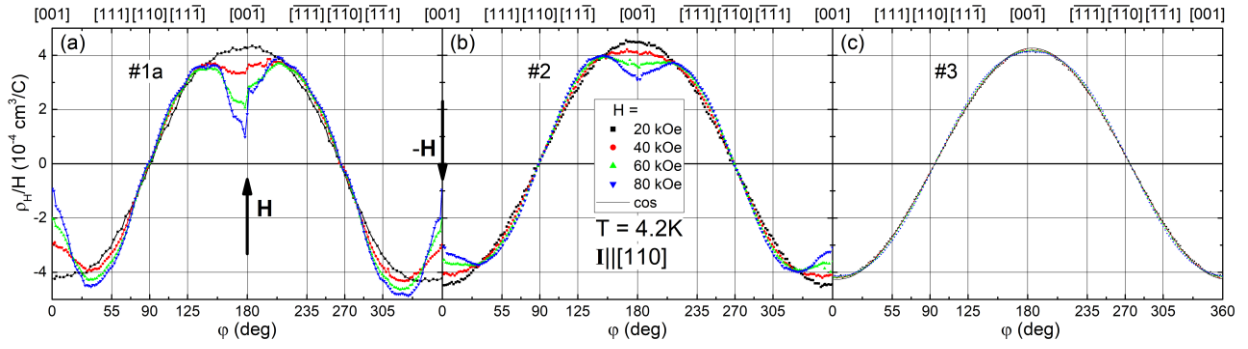


Fig.7

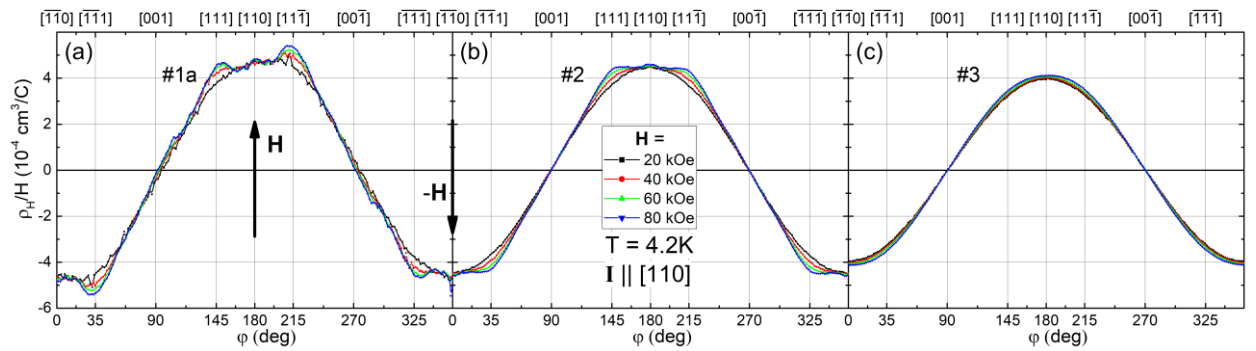


Fig.8.

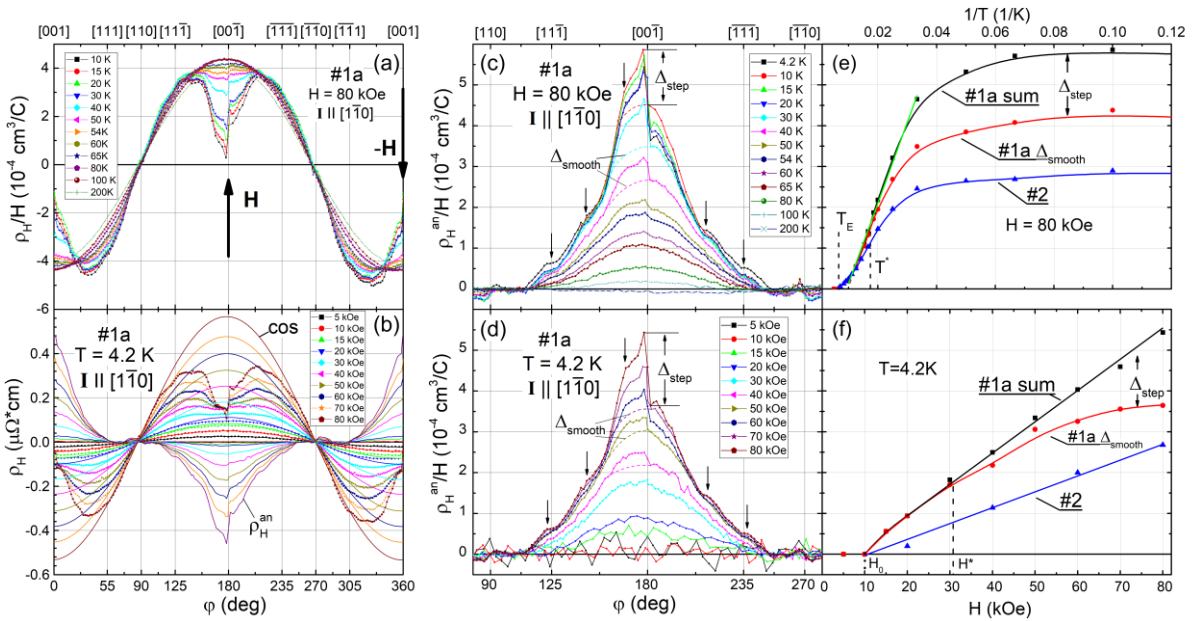


Fig.9.

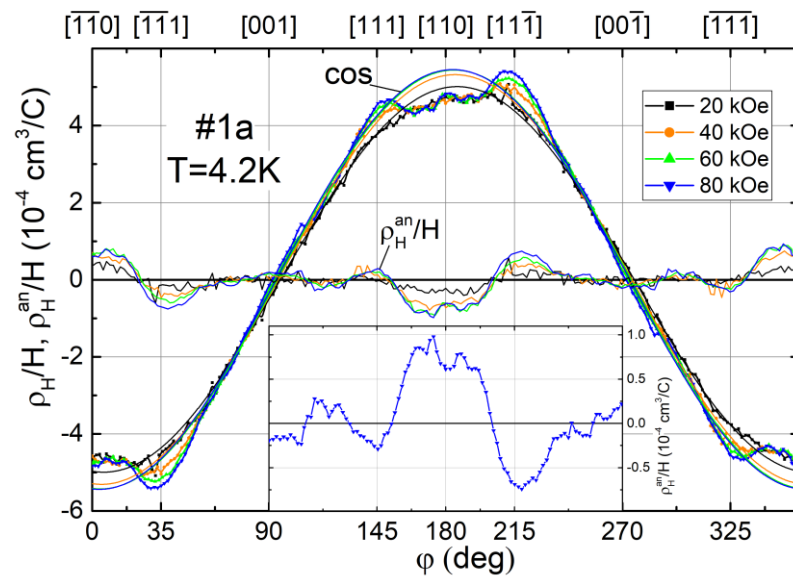


Fig.10.

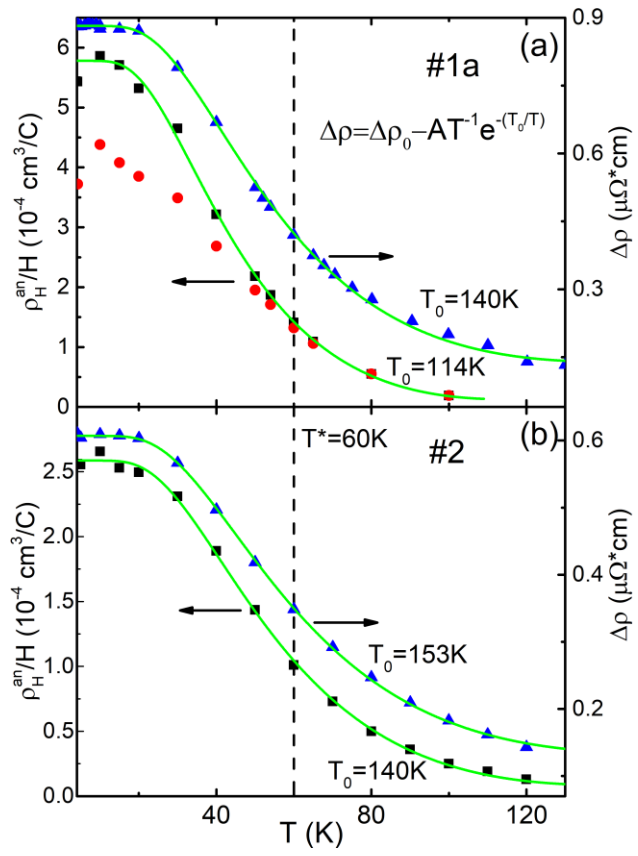


Fig.11.

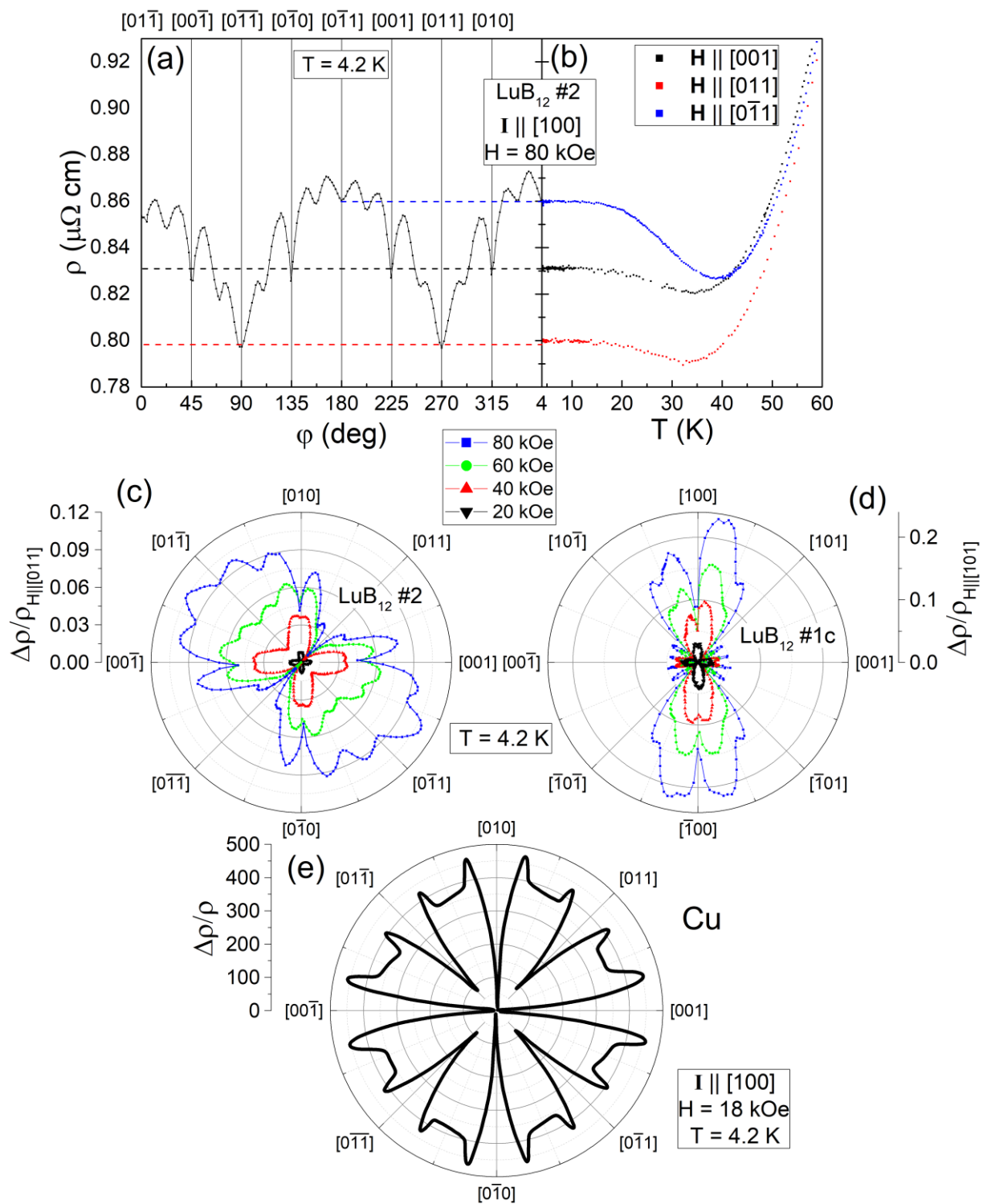


Fig.12.

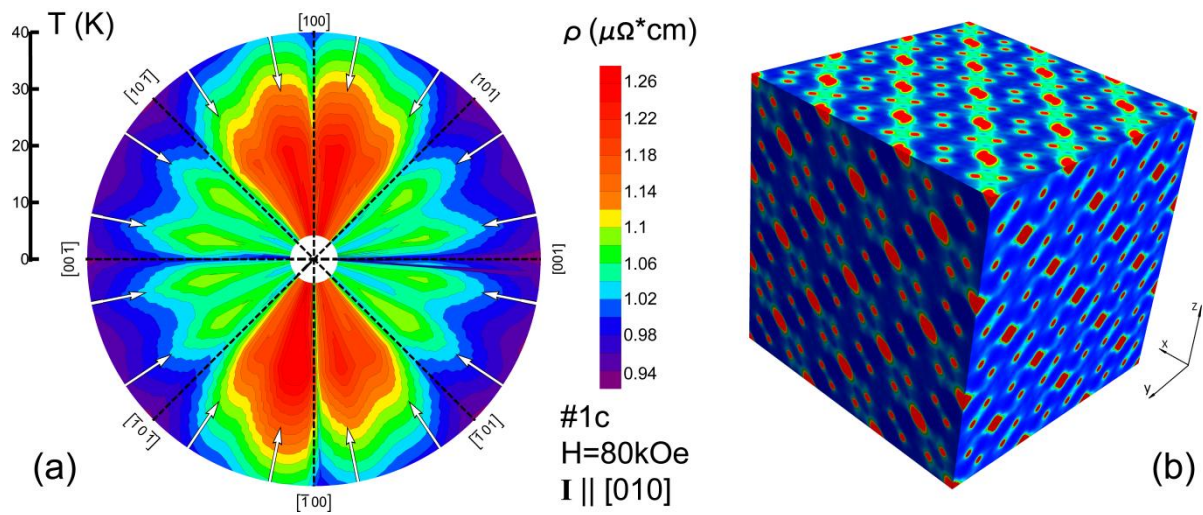


Fig.13.

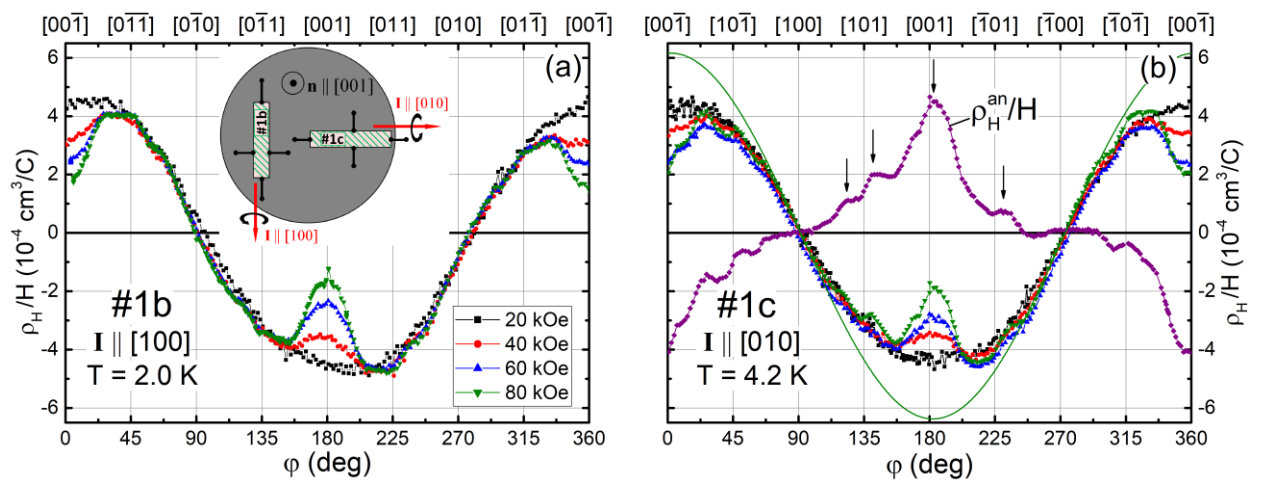


Fig. 14.

Supplementary Information

to the paper of N. Sluchanko, A. Azarevich, A. Bogach, S. Demishev, K. Krasikov, V. Voronov,
V. Filipov, N. Shitsevalova, V. Glushkov

“Hall effect and symmetry breaking in non-magnetic metal with dynamic charge stripes”.

1. The crystal growth.

Lu₂O₃ powder was preliminarily annealed at 800⁰C for 2 hours to remove the crystallization water, after that the charge was prepared from oxide and boron according to the equation of a solid-state reaction of the borothermal reduction:



The prepared charge was mechanically mixed for several days, no less than 5 times being sifted through a sieve in order to break conglomerates based on oxide and boron. It was necessary to prepare, as far as possible, a homogeneous mixture. The prepared mixture was compressed into tablets with a diameter of 15 mm and a height of 10 mm, which were aged in a vacuum furnace for an hour at a temperature of 1650⁰C. Since the solid-phase synthesis is determined by the diffusion of boron into oxide particles, then to obtain a homogeneous composition, the sintered tablets were broken, pressed again and kept in vacuum at 1750⁰C for an hour. The annealed tablets were again broken; the powder was cold pressed into rods with a diameter of 8 mm and a length of 60 mm and sintered for one hour at 1750⁰C in vacuum. The final homogenization occurs in the melt in the process of crystal growth.

The synthesis, annealing of tablets and sintering of rods took place in the same crucibles from ZrB₂. The melting temperature of ZrB₂ is ~ 3000⁰C; therefore, contamination with crucible material is excluded. Thus, the initial LuB₁₂ rods for crystal growth were identical in composition and purity. Volatile impurities present in boron are removed during the synthesis and zone melting, and in the grown crystals according to the optical spectral analysis the amount of impurities does not exceed 10⁻³ mass % (except for RE); rare earth impurities are determined by the purity of the starting lutetium oxide, the total content of the concomitant RE impurities is not more than 1.5 10⁻³ %.

Zone melting is carried out in a closed chamber under the pressure of high-purity argon (volume fraction of argon is not less than 99.993 %). The process of the chamber preparing for melting is also identical for all crystals. Preliminarily the chamber is pumped out to 10⁻³ mm Hg (0.1333 Pa), then it is filled with argon up to 0.2 MPa and again is pumped out, after which it is filled with argon to a predetermined pressure, and the melting process begins.

In the case of the crystal No. 1, an additional purification of argon from possible impurities of other gases was carried out directly in the growth chamber, whose presence cannot be excluded given their partial pressures, whatever the quality of the system sealing. Oxygen is especially undesirable as it promotes the growth of block crystals. Ti was used as a getter. In addition, during the growth of this crystal, both the feeding rod and the growing crystal rotated in opposite directions at rates of 10 and 4 rpm, respectively, which favored to a more uniform temperature distribution in the melt zone and equalization of the crystallization front, reducing thermal and mechanical stresses in the crystal. This crystal was grown with one pass, under a pressure of Ar 0.5 MPa, the seed was fixed in the upper shaft, and linear velocities were 0.5 and 0.4 mm/min for the growing crystal and the feeding rod respectively. The Laue photo (not presented) demonstrated the absence of split-in of the reflexes, i.e. a mosaity structure was not detected and a quality single crystal was grown.

Over time, we refused from additional gas purification, since the split-in of reflexes at the Laue photos of the grown crystals was absent as before.

The remaining crystals, with the exception of crystal #3 with three zone passes, were also grown with one pass. The crystallization rates of all crystals differ slightly.

Crystals #2 and #4 were grown under identical conditions, the seed was fixed in the lower shaft, only the feeding rod rotated (5 rpm), the crystallization rate was slightly lower (0.45 mm/min), but the pressure in the chamber was reduced (0.2 MPa), in order to facilitate purification from volatile impurities from boron, and a piece of sintered boron was added to the initial zone to somewhat lower the temperature of the melt zone and achieve a more stable growth process. According to [S1] the boron predominant evaporation resulted in a shift of the composition within the homogeneity region to a side rich in lutetium, i.e. the formation of defects in the boron sub-lattice, which led to an increase in residual resistance. This did not affect the quality of the Laue photos.

In the case of sample #5, the pressure in the chamber was further reduced ($P = 0.15$ MPa), and, accordingly, the concentration of defects in the boron sub-lattice was increased.

Crystal #3 was melted three times, the pressure in the chamber was 0.2 MPa at each pass, the rate of movement of the crystallizing ingot was 0.45 mm/min, giving 0.4, 0.42, 0.42 mm / min, and its rotation rate was 3, 5, 5 rpm / min., respectively. The grown ingot was much stressed, the end of the zone was in small cracks, but the Laue photo at a distance of 5 mm from the end of the crystal zone was very good. Thus, mechanical stresses, as a result of deviations from stoichiometry caused by three-fold re-melting and temperature gradients at the melt-to-crystal interface worsened the real structure of the crystal and increased residual resistance, but this did not affect the macrostructure.

Thus, indirectly, based on the values of the residual resistance, the influence of the production conditions on the quality of the grown crystals is detected. Unfortunately, the error in the determination of boron concentration by analytical methods is very large and it was not possible to determine the exact composition of the grown crystals.

[S1] Shitsevalova N. Magnetic, thermal and transport properties of rare earth dodecaborides. *PhD Thesis*, Institute of Low Temperature and Structure Research of Polish Academy of Sciences, Wroclaw, 166 pp. (2001)

2. Supplementary information to the results of the charge transport in LuB₁₂.

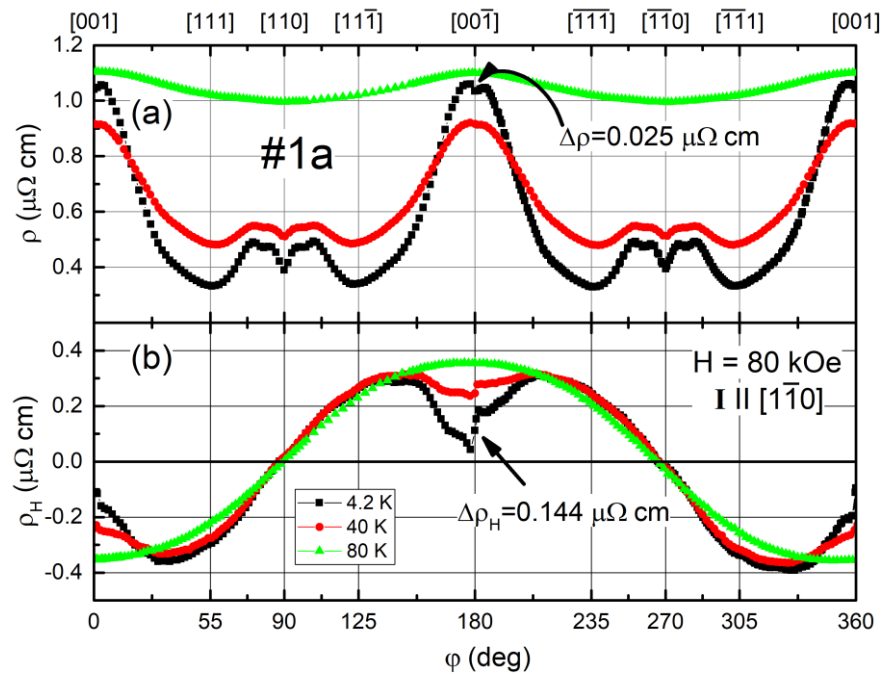


Fig.S1. Comparison of the amplitude of the resistivity and the Hall resistivity anomalies on the angular dependences near $\mathbf{H} // \mathbf{n} // \langle 001 \rangle$ in LuB₁₂ (#1a) at the temperatures 4.2-80 K.

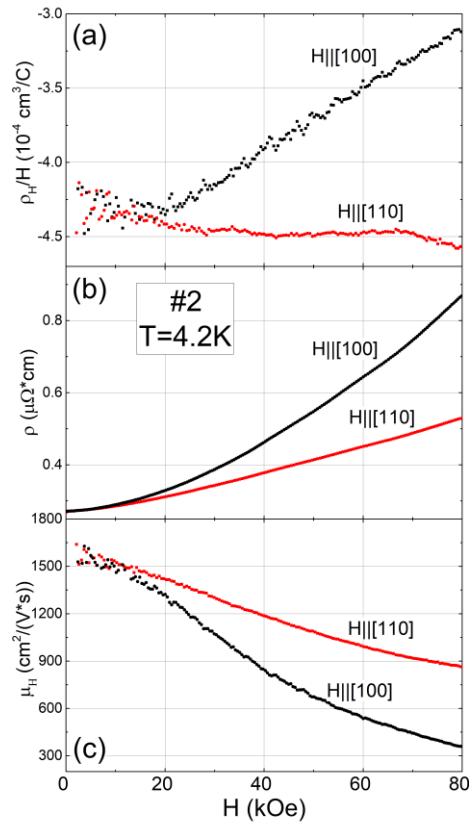


Fig.S2. Magnetic field dependences of (a) the reduced Hall resistivity ρ_H/H , (b) resistivity and (c) Hall mobility in LuB_{12} (#2) at $T=4.2$ K.

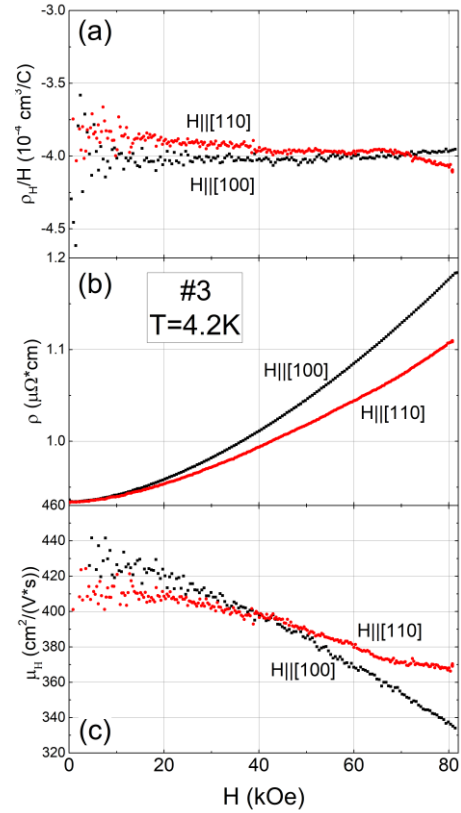


Fig.S3. Magnetic field dependences of (a) the reduced Hall resistivity ρ_H/H , (b) resistivity and (c) Hall mobility in LuB_{12} (#3) at $T=4.2$ K.

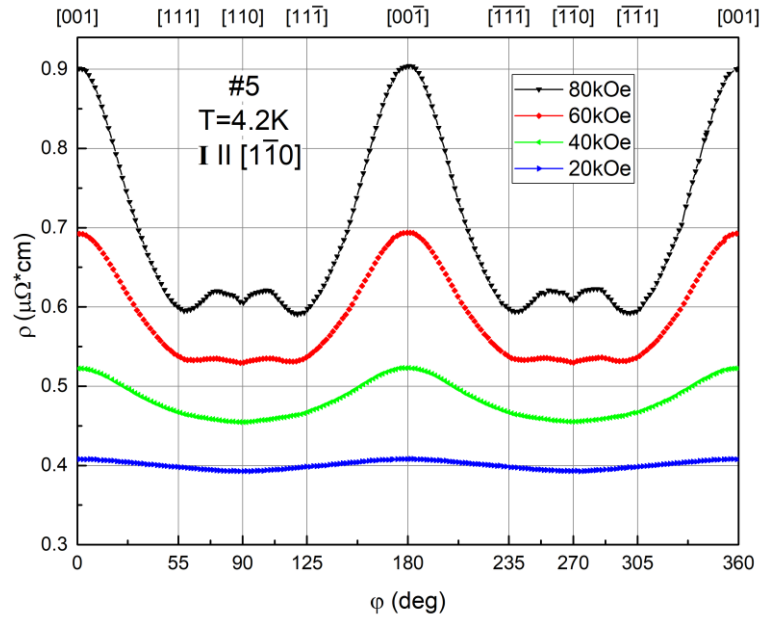


Fig.S4. Liquid helium angular dependences of resistivity in the LuB_{12} (sample #5, $\mathbf{I} // [1-10]$).

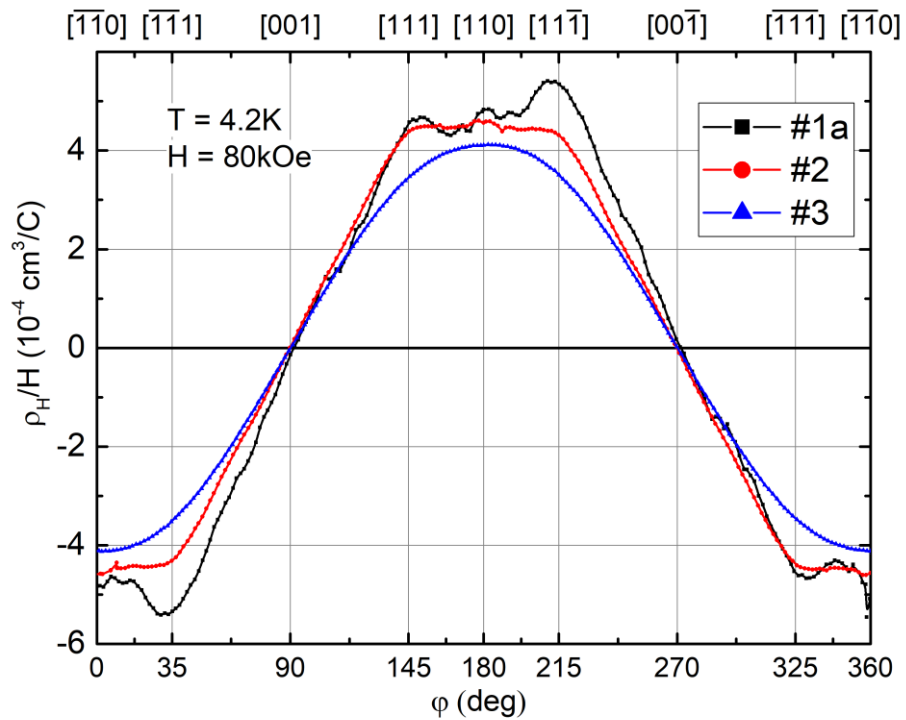


Fig.S5. The comparison of the reduced Hall resistivity angular dependences for the samples #1, #2 and #3 of LuB_{12} ($T=4.2\text{ K}$, $H=80\text{ kOe}$, $\mathbf{I} // [1-10]$, $\mathbf{n} // [110]$).

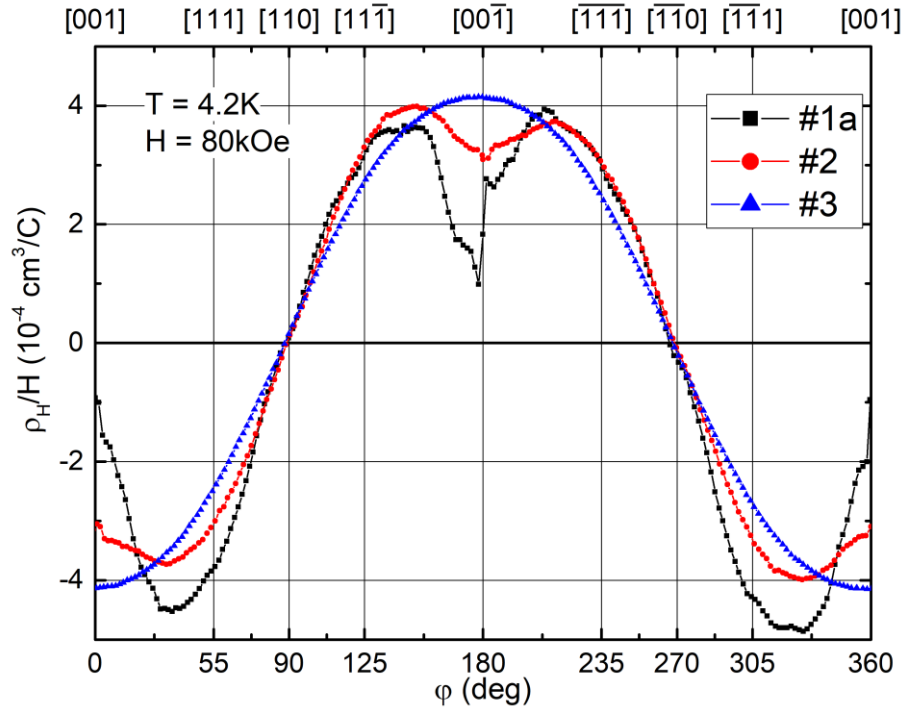


Fig.S6. The comparison of the reduced Hall resistivity angular dependences for the samples #1, #2 and #3 of LuB_{12} ($T=4.2\text{ K}$, $H=80\text{ kOe}$, $\mathbf{I} \parallel [1-10]$).

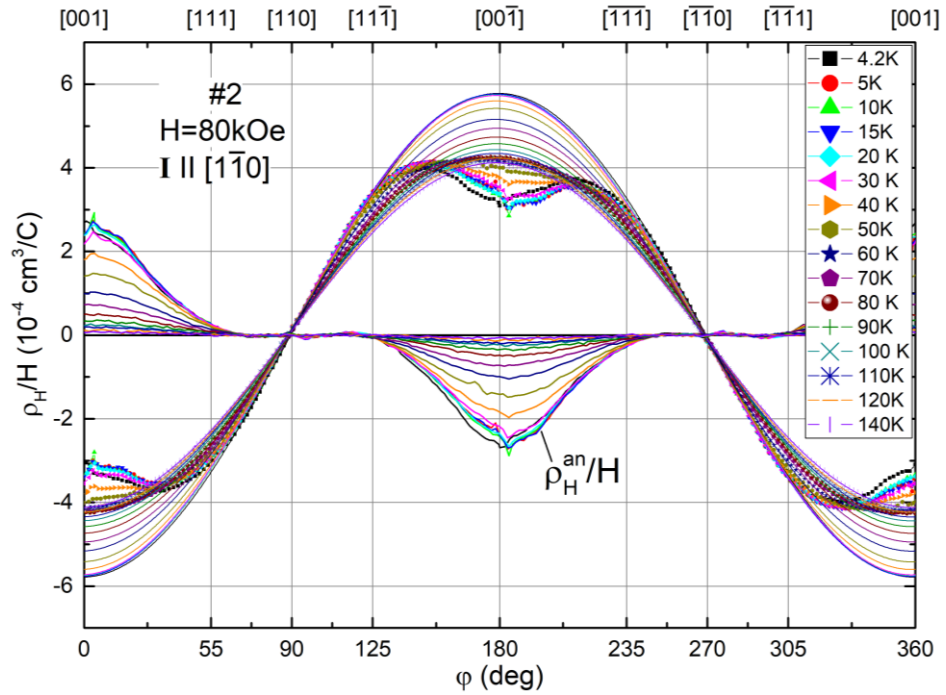


Fig.S7. The separation of the ordinary (cosin-type) and anomalous components in the reduced Hall resistivity at temperatures in the range 4.2-140 K at $H=80\text{ kOe}$ for the sample #2 of LuB_{12} ($\mathbf{I} \parallel [1-10]$).

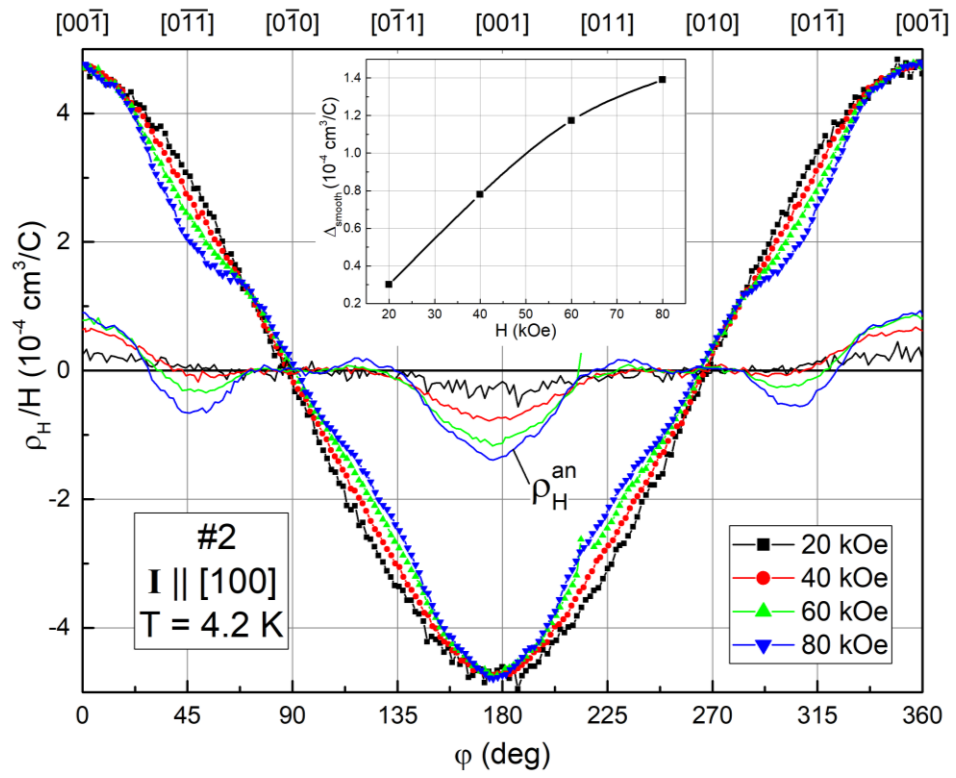


Fig.S8. The separation of the ordinary (cosin-type) and anomalous components in the reduced Hall resistivity at $T=4.2$ K and in the range $H \leq 80$ kOe for the sample #2 of LuB_{12} ($\mathbf{I} \parallel [100]$). Inset shows the amplitude of the anomalous contribution $\Delta_{\text{smooth}}(H)$.

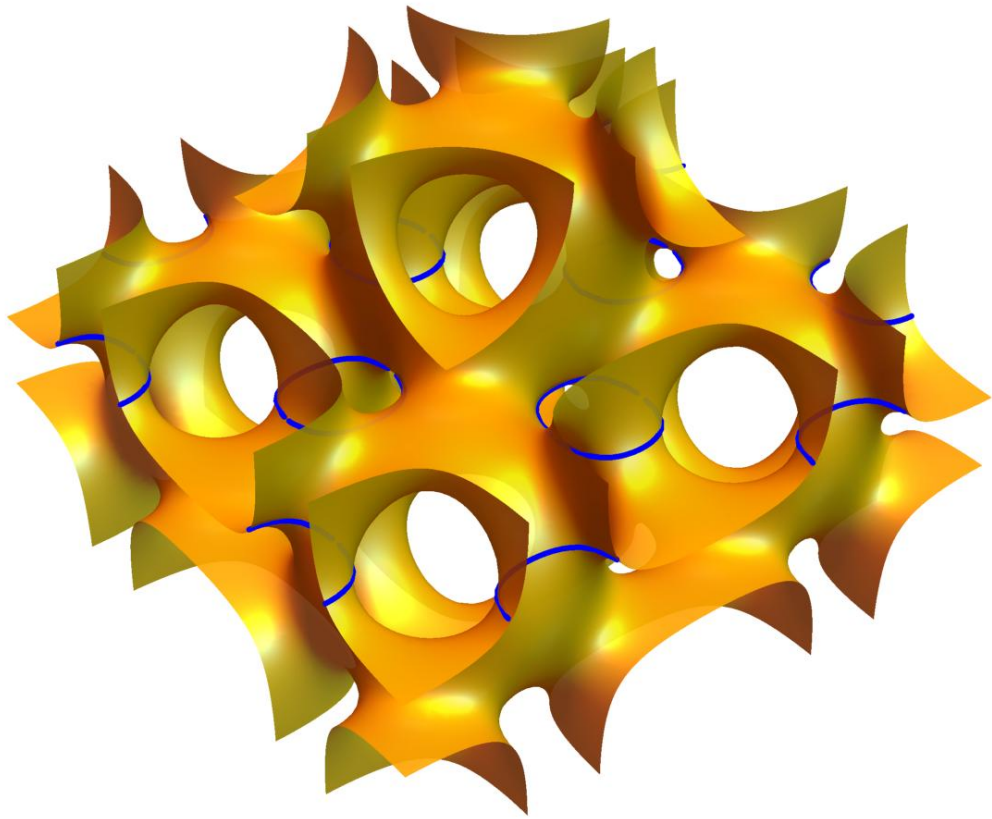


Fig.S9. The hole-like Fermi surface sheet in LuB_{12} . Solid blue lines show the four cornered rosettes (R_{001} orbit (SdH α_2 branch), see text for more detail).

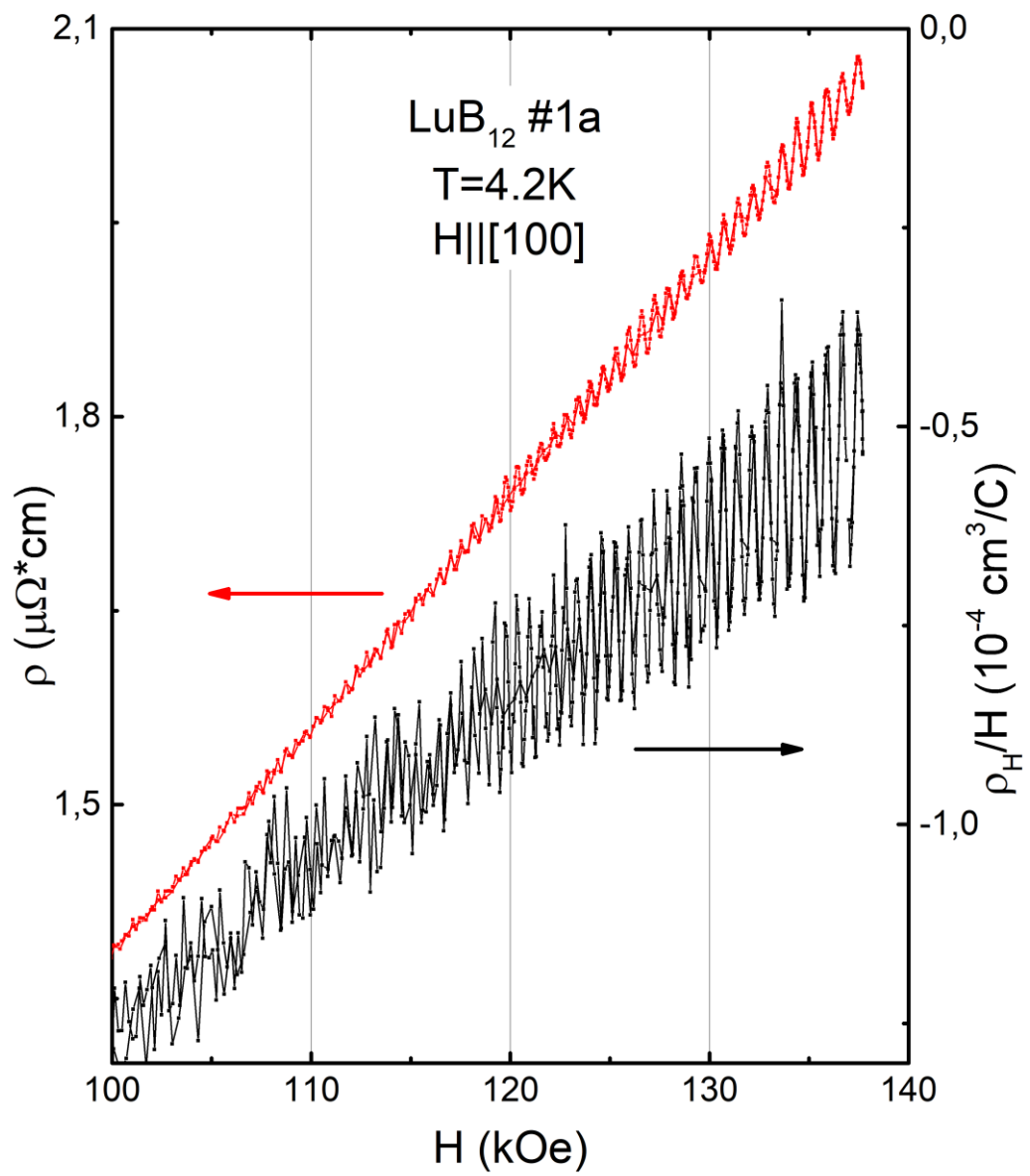


Fig.S10. Quantum oscillations of resistivity and the reduced Hall resistivity in LuB_{12} (sample #1a).